MACQUARIE
University
SYDNEY·AUSTRALIA

CALCIUM SIGNALLING IN TDP-43 MODELS OF MOTOR NEURONE DISEASE AND FRONTOTEMPORAL DEMENTIA

Gabriella Chan

B. Sc. (Hons)

Supervisor: A/ Prof. Yazi Ke

Co-supervisor: Dr. Annika van Hummel

A thesis submitted in Partial Fulfillment of the Requirements for the Degree of

Master of Research

Macquarie University

Faculty of Medical and Health Sciences

Department of Biomedical Sciences

Dementia Research Centre

October 2019

Contents

List of tables

List of figures

Abstract

Motor neurone disease (MND) and frontotemporal dementia (FTD) are terminal neurodegenerative diseases, with rapid disease progression. Clinically, patients present with overlapping symptoms, and the diseases share underlying genetic features and pathophysiology. Notably, pathological changes in neuronal excitability and calcium dynamics have been reported in disease. Furthermore, these signalling changes are implicated in neuronal death present in motor neurone disease and frontotemporal dementia. However, the current literature is unclear as to the nature of these excitability changes, with some studies suggesting that hyperexcitability leads to excitotoxicity, while others suggest that hypoexcitable neurons are most vulnerable to neurodegeneration.

The present study presents two complementary models for investigation of calcium signalling changes in disease and reports on preliminary findings as proof of concept. Firstly, signalling changes were identified in an *in vitro* model of disease, by co-transducing primary hippocampal neurons with variants of the disease related protein TDP-43 together with the fluorescent calcium sensor jGCaMP7f. Calcium activity was then recorded in a TDP-43 mouse model of disease using the Miniscope miniaturised microscope system. This Miniscope application in a neurodegenerative disease mouse model is the first of its kind in this field. In these models TDP-43 expression reduced calcium response during spontaneous neuronal spiking activity, while increasing signalling synchronicity. These changes occurred through increased sensitivity to neuronal stimulation as well as decreased response to repeat stimulation, suggesting a complex and nuanced relationship between excitability and neurodegeneration. Together, these models provide a promising platform for further study of MND and FTD pathomechanisms.

Abbreviations

AAV	adeno-associated virus
AMPAR	AMPA receptor
bvFTD	behavioural variant FTD
BSA	bovine serum albumin
Ca^{2+}	calcium
CSF	corticospinal fluid
CTCF	corrected total cell fluorescence
CNMF	constrained non-negative matrix factorization
DAPI	4',6-diamidino-2-phenylindole
DAQ	data acquisition board
DIV	days *in vitro*

EAAT2	excitatory amino acid transporter 2
EEG	electroencephalography
ER	endoplasmic reticulum
FBS	fetal bovine serum
FOV	field of view
FPS	frames per second
FTD	frontotemporal dementia
ICC	immunocytochemistry
iPSC	induced pluripotent stem cell
LCD	low complexity domain
LMN	lower motor neuron
MEP	motor evoked potential
MND	motor neurone disease
MOI	multiplicity of infection
mPTP	mitochondrial permeability transition pore
N2a	Neuro-2a
NES	nuclear export signal
NLS	nuclear localisation signal
NMDAR	NMDA receptor
OASIS	Online Active Set method to Infer Spikes
PBS	phosphate buffered saline
PFA	paraformaldehyde
pTDP-43	phosphorylated TDP-43
rfu	relative fluorescence units
ROI	region of interest
ROS	reactive oxygen species
RRM2	RNA recognition motif 2
SICI	short interval intracortical inhibition
TMS	transcranial magnetic stimulation
UMN	upper motor neuron
UPR	unfolded protein response
VGCC	voltage-gated calcium channel
WT	wild type

Declaration

The work presented in this thesis is an original piece of research which has not been previously submitted as part of the requirements for a degree or diploma in any university. All work done towards this thesis was completed while enrolled as an HDR candidate at Macquarie University. To the best of my knowledge and belief, the thesis contains no material previously published or written by another person except where due reference is made in the thesis itself.

This project was funded by the Macquarie University Research Excellence Scholarship for Master of Research (MQRES-MRES No. 20191185). Work with presented in this thesis was approved by the relevant authorities under the following reference numbers:

Institutional Biosafety Committee:
0347 - Cell lines and primary cells for studies into neurodegenerative diseases
0335 - Gene modification – studies into the physiology and pathology of the nervous system

Animal Ethics Committee:
2018/019 - Neurodegeneration protocol: investigating disease mechanisms and development of new therapies

Gabriella Chan

Statement of Contributions

Adeno associated virus (AAV) hSynapsin TDP-43 myc-tagged variants were provided by Dr. Wei Siang Lee. pGP-AAV-syn-jGCaMP7f-WPRE was a gift from Douglas Kim & GENIE Project (Addgene plasmid # 104488; http://n2t.net/addgene:104488; RRID:Addgene_104488). pAAV-CAGmRuby2 was a gift from Viviana Gradinaru (Addgene plasmid # 99123; http://n2t.net/addgene:99123; RRID:Addgene_99123). pAAV TDP-43 mRuby2 variants were cloned with help from Mr Mehul Gajwani. All AAVs used in this project were produced by Ms. Yijun Lin of the Dementia Research Centre Viral Core.

Primary hippocampal cultures used in this project were prepared by Dr. Carol Au, Ms. Holly Stefen and Ms. Esmeralda Paric of the Neuronal Culture Core Facility (NCCF, Macquarie University). Animal care and genotyping was provided by Mr. Troy Butler, Ms. Jess Spathos and the Central Animal Facility (CAF, Macquarie University).

Acknowledgements

I would firstly like to thank Prof. Lars Ittner, director of the Dementia Research Centre (DRC). Thank you for welcoming me into the DRC, and for sharing your brilliant project ideas and insights. I would also like to thank my supervisors A/ Prof. Yazi Ke and Dr. Annika van Hummel for their immense patience and guidance over the course of this project. Without your constant support, I certainly would not have completed this thesis. Finally, I would like to thank all members of the DRC. Thanks for your advice, your willingness to lend a hand, and most of all for your friendship.

1 Introduction

1.1 Motor Neurone Disease and Frontotemporal Dementia

Motor neurone disease (MND) and frontotemporal dementia (FTD) are debilitating neurodegenerative diseases with rapid disease progression which invariably results in death. The average age of diagnosis for MND is 59 years, with average life expectancy of 3 years after diagnosis and, in Australia, MND has a prevalence of 8.7 per 100,000 (Deloitte, 2015). FTD is the second most common cause of early-onset dementia, with average diagnosis at around 60 years of age, and life expectancy of 5 years after diagnosis. FTD prevalence is estimated at around 15-50 per 100,000 Australians (AFTDA, 2017). Despite hundreds of clinical trials, there is no cure available for either disease and current treatments merely extend life expectancy by a matter of months (NIH, 2017; Carbone et al., 2012; Rothstein, 2017).

In MND, patients present initially with weakness in the limbs, or facial weakness and slurred speech, depending on site of disease onset. In either case, patients experience rapidly progressing muscle atrophy, which leads to increasing levels of paralysis, respiratory dysfunction, and eventually death (Picher-Martel et al., 2016). In FTD, patients may initially present with either changes in personality and social behaviours, or language decline, which then progresses to severe cognitive decline. Furthermore, in later stages of FTD, patients commonly present with motor symptoms and muscle rigidity, as in MND. Similarly, up to half of MND patients experience mild cognitive impairment or behavioural changes, and approximately 15% of patients eventually meet the diagnostic criteria for both diseases (MND-FTD; Ringholz et al., 2005; Tan et al., 2017). Initial symptomatic heterogeneity meant that MND and FTD were historically considered to be separate diseases. However, due to clinical overlap and similarities in underlying genetics and pathomechanisms, MND and FTD are now recognised as existing on a motor neurone disease-frontotemporal dementia continuum (Burrell et al., 2016).

1.2 Pathology and pathomechanisms of MND/FTD

1.2.1 Genetics of MND and FTD

Familial disease history is by far the most significant risk factor for MND and FTD. Genetic mutations are the only known cause of MND, whether they be sporadic or familial, and 40% of

FTD cases have some degree of heritability (Ling et al., 2013; Forrest et al., 2019). Several genes have been related to both MND and FTD, most notably *C9ORF72* and *TARDBP*, where pathological mutations may cause either disease. Mutations in *C9ORF72* are the most common genetic abnormality in both familial MND and FTD, causing 23.5% and 11.7% of cases respectively (Renton et al., 2011, DeJesus-Hernandez et al., 2011). Mutations in the *TARDBP* gene, encoding the TDP-43 protein, are less common, occurring in around 3% of patients, however they form a significant part of protein pathology in most MND and FTD cases. There are also disease-specific mutations, including mutations in *SOD1* which cause MND, and *MAPT*, which encodes the microtubule associated protein tau, which causes FTD (Lagier-Tourenne and Cleveland, 2009).

1.2.2 Neuropathology of MND and FTD

Upon post-mortem examination, patient brains reveal aberrant protein aggregates, and targeted neurodegeneration. In 2006, Neumann and colleagues identified these protein aggregates as being comprised of misfolded and hyperphosphorylated TDP-43 in 90% of MND, and 45% of FTD cases. In remaining MND cases protein aggregates contain the SOD1 or FUS proteins, while protein aggregates containing tau, FUS, and UPS have been identified in FTD (Ling et al., 2013). These protein aggregates are known to be ubiquitinated, hyperphosphorylated, and exhibit cytoplasmic mislocalisation in disease.

As disease state progresses, phosphorylated protein aggregates can be seen to progress in a sequential, stereotypic manner. In MND patients with low disease burden, phosphorylated TDP-43 (pTDP-43) pathology is present in the motor cortex, brainstem, and spinal cord, while in later disease pTDP-43 can also be found in the frontal and temporal lobes (Brettschneider et al., 2013). In behavioural variant FTD (bvFTD) with TDP-43 pathology, pTDP-43 inclusions are first apparent in the prefrontal cortex and amygdala, which then spreads to the frontal and temporal lobes (Brettschneider et al., 2014).

1.3 Current models of MND/FTD

While the clinical and pathological progression of MND and FTD have been well characterised, the underlying disease mechanisms remain unclear. As such, these clinical observations are used to design disease models which recapitulate disease phenotype. A variety of model systems have been generated which make use of key protein features implicated in MND-FTD. These offer opportunities for deeper interrogation of disease mechanisms, which are ultimately translated back into a disease context. No single model perfectly captures the disease state, so

models are used in combination to build a complex and layered understanding of disease. These can be largely separated into two main categories; *in vitro* models and *in vivo* models.

1.3.1 *In vitro* and *in vivo* models

True neuronal cell culture models of MND and FTD cannot be maintained, as mature human neurons do not proliferate. Therefore, neuronal cell lines used in MND-FTD studies are typically from one of three assays; either immortalised cell lines derived from tumour biopsies, primary neuronal cultures from animals, or induced pluripotent stem cells (iPSCs) derived from patient samples. These *in vitro* cultures share many of the same advantages and disadvantages, with overlapping use cases (summarised in Table 1). They have a niche as a first stage screening tool, whether that be in understanding biomolecular mechanisms, drug candidates, or disease mutations. However, they tend to model embryonic rather than adult neurons, and are limited in their ability to represent the true intricacy of human disease.

Animal models are used to provide a more nuanced picture of human disease and are better able to model complexities of the disease state. As models progress from basic invertebrate *in vivo* models to vertebrate and mammalian systems, they more accurately model the biomolecular mechanisms in human disease. The most common invertebrate species used in MND-FTD animal studies are *Caenorhabditis elegans* and *Drosophila melanogaster*, which exhibit gradual impairments in locomotion and reduced lifespan with gene knock-out or mutant gene expression. However, these have limited similarities to the human nervous system structure, and entirely fail to model behavioural characteristics of FTD (Therrien & Parker, 2014; Casci & Pandey, 2015). The zebrafish (*Danio rerio*) provides an intermediate vertebrate model with the significant advantage of transparency throughout its developmental stages. While this is of great benefit in imaging studies, the nervous system structure of the zebrafish lacks the corticospinal and rubrospinal tracts essential for modelling upper motor neuron dysfunction (Babin, Goizet & Raldua, 2014). Rodent models (*Rattus norvegicus*, and *Mus musculus*) share remarkable similarities with humans in their central nervous system architecture and cortical structure, and as such are by far the most common model of MND-FTD. Moreover, of these most commonly used animal models, they are the best model of behavioural changes and memory deficits observed in MND-FTD. As such, mouse models provide the best translation to the clinical disease state and constitute two-thirds of all animal studies in MND-FTD (Tan et al., 2017; summarised in Table 1).

Table 1: Summary of the most common in vitro and in vivo models used in MND/FTD research

	Model	Strengths	Weaknesses	Applications	References
In vitro	Neuroblastoma cells	Cheap, robust, and easy to maintain, retain many neuron-like qualities.	Not true neurons, they have an altered physiological profile.	Screening tool, validating *in vivo* findings.	Zhong et al., 2008; Gal et al., 2011.
In vitro	Primary neuronal cultures	Versatile neurons which may be derived from any tissue type.	Difficult preparations, ethical issues. Necessarily derived from animal cells.	Small molecule screens, identifying potential familial mutations.	Durham et al., 1997; Bigini et al., 2002.
In vitro	Induced pluripotent stem cells	Human neurons which may be derived from patient cells.	Phenotypic variability between lines. These model the early disease state.	Modelling interactions between cell populations. Drug candidate screens.	Yang et al., 2013; Di Giorgio et al., 2008.
In vivo	*D. melanogaster*	Extremely fast reproductive cycle. Easy maintenance.	Different nervous system structure. Cannot model behavioural changes.	Modelling motor deficits in MND.	Casci & Pandey, 2015.
In vivo	*C. elegans*	As above, transparent, complete neuron connectivity map.	As above.	As above.	Therrien & Parker, 2014.
In vivo	*D. rerio*	Transparent larval stage facilitates imaging. Vertebrate model.	No corticospinal or rubrospinal tract. Limited to modelling motor deficits.	Modelling motor deficits in MND. Imaging *in vivo* neuronal activity.	Babin, Goizet & Raldua, 2014.
In vivo	*M. musculus*	Vertebrate model, similar cortical structure to humans.	Limited social repertoire, only models certain behavioural elements.	Modelling motor, anxiety and memory deficits in MND/FTD.	Tan et al., 2017.
In vivo	*R. norvegicus*	As above, with increased behavioural complexity and social behaviour.	One of the larger model animals, increased housing footprint and cost.	As above, with options to model social deficits.	Tan et al., 2017.

1.3.2 Functional and disease models

When leveraging these cellular or animal models for use in MND and FTD study, there are two common approaches taken to elucidate protein function, with some overlap between them. To understand the role of different elements of disease-related proteins, a functional approach may be taken, with gene knockouts, overexpression systems, or functional mutants. Alternatively, disease-mimicking mutants may be generated to model pathological behaviour. Here, models of TDP-43 dysfunction in MND and FTD will be summarised, due to the key role of TDP-43 in patient pathology. However, there exist a great many other disease models which investigate the roles of various disease associated proteins, including SOD1, C9ORF72, and FUS.

Several *TARDBP* knockout mouse models have been generated to investigate the effects of loss of TDP-43 function *in vivo*. In all cases complete TDP-43 knockout (*TARDBP*-/-) was shown to be incompatible with life, with embryonic lethality before E8.5, while heterogenous knockout mice (*TARDBP*+/-) showed little obvious pathology (Sephton et al., 2010; Wu et al., 2010). Moreover, conditional postnatal knockout of TDP-43 also led to rapid weight loss and death within 9 days (Chiang et al., 2010). Conversely, TDP-43 overexpression also led to rapid lethality across several mouse models. Notably, expression of wild-type human TDP-43 was sufficient to cause neuropathology and neuroinflammation in mice, with associated motor and behavioural deficits (Cannon et al., 2012; Igaz et al., 2011).

Functional elements in the TDP-43 protein have also been exploited, most notably, the nuclear localisation signal (NLS) a nuclear export signal (NES), which regulate intracellular localisation. Truncations of these elements have been used to simulate the mislocalisation and protein aggregates seen in disease. Expression of TDP-43 harbouring NES truncations (ΔNES) prevents the export of TDP-43 from the nucleus to the cytoplasm in cells, while expression of defective NLS (ΔNLS) in cells prevents re-entry from the cytoplasm into the nucleus, depleting nuclear TDP-43. In either case, disturbance of normal TDP-43 trafficking using ΔNES or ΔNLS leads to protein ubiquitination and aggregation modelling biochemical changes in MND-FTD (Winton et al., 2008). The ΔNLS mutation has been applied in several mouse models and, depending on the promoter used, its expression leads to a severe disease phenotype with motor neuron loss, muscle wasting, and early death (Walker et al., 2015; Igaz et al., 2011).

Disease-causing mutations have been identified in the TDP-43 protein in both familial and sporadic MND and FTD. These mutations are almost always dominantly heritable missense mutations and have largely been identified in the C-terminal glycine rich domain (Lagier-Tourenne & Cleveland 2009). Several of these variants have been replicated in cell and animal

models, leading to varying degrees of neuropathology and functional deficits (mouse models are summarised in Table 2). Since no single model perfectly recapitulates the disease state, each of these mutations provides valuable insights into normal and pathological protein function. Our group has previously published on an inducible TDP-43^{A315T} mouse model of MND-FTD (iTDP-43^{A315T}; Ke et al., 2015), under the neuronal specific mThy1.2 promoter. These animals expressed transgenic human TDP-43 at around 2-fold endogenous levels, which resulted in a progressive and severe disease phenotype recapitulating key aspects of MND and FTD. Notably, mice experienced behavioural deficits including disinhibition and memory loss, as well as muscle wasting and associated coordination deficits. On histological and biochemical examination, iTDP-43 mice presented with insoluble TDP-43 aggregates, as well as phosphorylated and ubiquitinated TDP-43 fragments, and progressive hippocampal and cortical atrophy.

Overall, many models of TDP-43 pathology in MND/FTD have been generated across multiple model systems. Characterisation of these models reveal that TDP-43 serves an essential role in normal function and is closely regulated, with perturbations in TDP-43 levels or protein structure leading to severe phenotypes. However, the underlying mechanisms and pathways behind these phenotypes are manifold and complex.

1.4 Excitotoxicity and calcium

With so many disease pathways and potential mechanisms implicated in MND/FTD, it remains an active research question as to how these mechanisms are related. Calcium dysfunction presents a common theme between many of these mechanisms, including ER stress, changes in the unfolded protein response (UPR), excitotoxicity, and oxidative stress, amongst others. Currently, research into calcium dysfunction in MND/FTD centres around two main concepts. Firstly, changes in intracellular calcium buffering are suspected to induce neuronal excitotoxicity. Secondly, calcium influx is also essential in action potential initiation, which appears to be impaired in disease.

1.4.1 Extracellular glutamatergic signalling

Intracellular calcium disturbances in MND/FTD may be traced back to glutamatergic signalling and reuptake disturbances. In both patients and mouse models of MND, synaptosomes isolated from the spinal cord showed a decrease in glutamate transport velocity and uptake (Battaglioli et al., 1993; Rothstein et al., 1992). Similarly, an increase in glutamate has been observed in the CSF of patients with C9ORF72 repeat expansions (Shaw et al., 1995; Shi et al., 2018). Both

Table 2: Summary table of selected rodent TDP-43 models of MND and FTD. Functional and genetic mutations under various promoters show differing degrees of neuropathology and functional deficits.

Promoter	TDP-43 mutation	Description	Neurodegeneration		Motor deficits	Premature death	Reference
			UMN	LMN			
mPrp	WT	Transgenic full-length human TDP-43	N	N	Y	Y	Xu et al., 2010
mThy1.2	WT	Transgenic full-length human TDP-43	Y	Y	Y	Y	Wils et al., 2010
CAMKIIα	ΔNLS	Transgenic human TDP-43 with truncated NLS	Y	N	Y	N	Igaz et al., 2011
NEFH	ΔNLS	Transgenic human TDP-43 with truncated NLS	Y	Y	Y	Y	Walker et al., 2015
TDP-43	F210I	Endogenous TDP-43 harbouring F201I mutation in RRM2 region	- [1]	N	N	N	Fratta et al., 2018
mPrp	A315T	Transgenic full-length human TDP-43 harbouring familial mutation	N	N	Y	Y	Stallings et al., 2010
mThy1.2	A315T	Transgenic full-length human TDP-43 harbouring familial mutation	Y	N	Y	N	Ke et al., 2015
TDP-43	M323K	Endogenous TDP-43 harbouring M323K mutation in LCD	- [1]	Y	Y	N	Fratta et al., 2018
TDP-43	Q331K	Point mutation knock-in equivalent to human Q331K mutation	Y	N	N	Y[2]	White et al., 2018
mThy1.2	M337V	Transgenic full-length human TDP-43 harbouring familial mutation	Y	Y	Y	Y	Janssens et al., 2013
TDP-43	G348C	Transgenic full-length human TDP-43 harbouring familial mutation	N	N	Y	N	Swarup et al., 2011

[1] No data, [2] Mutation may lead to premature death of male embryos.

UMN = upper motor neuron, LMN = lower motor neuron, NLS = nuclear localisation sequence, RRM2 = RNA recognition motif 2, LCD = low complexity domain.

MND and FTD patients exhibit dramatic and selective loss of the astrocytic excitatory amino acid transporter 2 (EAAT2, also known as GLT-1) which is necessary for clearance of synaptic glutamate (Fray et al., 2003; Tollervey et al., 2011). Abnormal EAAT2 mRNAs have been identified in patient brains concurrent with other neuropathology and are also detectable in the CSF early in disease (Lin et al., 1998). Interestingly, riluzole, the only drug approved for MND use in Australia, is known to elevate EAAT2 activity, inactivate voltage-gated sodium channels and is suspected to interrupt glutamate release (Carbone et al., 2012; Benavides et al., 1985).

Increased extracellular glutamate levels cause disturbances in glutamate neurotransmission, activating NMDA and AMPA receptors. While these are both typically calcium impermeable, the calcium permeability of AMPA receptors is determined by the presence or absence of the GluR2 subunit. AMPA receptors containing at least one GluR2 subunit in a tetramer are rendered impermeable to calcium, while receptors lacking GluR2 are highly calcium permeable. As synapses mature, calcium permeable AMPA receptors are replaced by calcium impermeable GluR2 containing AMPA receptors, in an astrocyte-mediated fashion (Blanco-Suarez et al., 2018). A single arginine in the GluR2 subunit is responsible for maintaining low calcium permeability, and transgenic mice have been generated encoding an asparagine at this site, which allows constant calcium permeability. Van Damme and colleagues (2005) demonstrated that functional modification of this charge to allow calcium entry was enough to cause progressive neurodegeneration, motor decline, and decrease survival in mice, modelling deficits seen in disease. Thus, alterations in synaptic glutamatergic signalling in MND/FTD increase calcium influx, leading to disease pathology (Fig. 1).

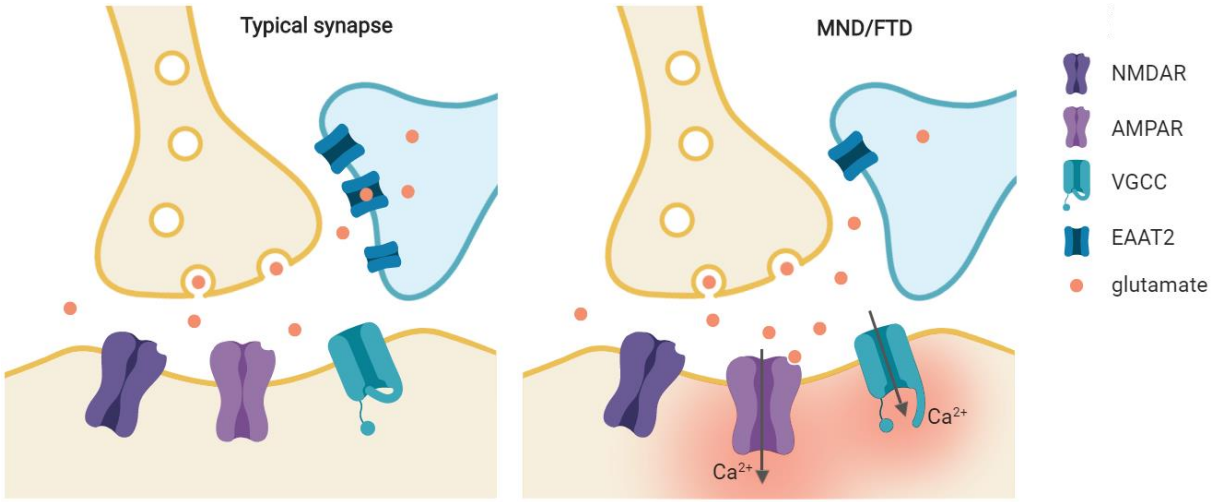

Figure 1: Synaptic dysregulation in MND/FTD leads to calcium influx and vulnerability to excitotoxicity in disease.

NMDAR = NMDA receptor, AMPAR = AMPA receptor, VGCC = voltage-gated calcium channel, EAAT2 = excitatory amino acid transporter 2.

1.4.2 Intracellular calcium dysfunction

Calcium serves as an essential intracellular messenger molecule, and intracellular calcium is tightly regulated at levels 10^4 times lower than extracellular calcium. Intracellular calcium homeostasis is maintained through calcium transport proteins, as well as intracellular calcium stores in the endoplasmic reticulum. (ER; Bagur & Hajnóczky, 2017). However, in both patient neurons and animal models, low cytosolic calcium buffering capacity has been observed. For instance, motor neurons have been shown to have a 5 times lower calcium buffering capacity than protected neuronal populations in mouse models (Palecek et al., 1999). Furthermore, patient neurons exhibit a reduction in calcium binding proteins such as parvalbumin and calbindin-D28K (Alexianu et al., 1994). Together these results suggest that a vulnerability to calcium toxicity presents as a significant risk factor in MND-FTD.

The primary intracellular store in the ER, which maintains ~10^3 times higher calcium than the cytoplasm. Additionally, the ER also responds to calcium dependent stimuli and serves essential roles in protein folding. However, formation and aggregation of pathological protein inclusions, such as those found in MND and FTD, leads to increased ER stress (Hetz & Saxena, 2017). Additionally, ER stress may also be induced by disturbance of ER calcium homeostasis, as calcium is required for correct protein subunit folding and export (Oakes & Papa, 2015). In either case, ER stress triggers activation of the UPR, which leads to adaptive neuronal plasticity under normal conditions. In neurodegenerative disease however, neurons display chronic accumulation of ER stress which leads to a maladaptive, terminal UPR culminating in neuronal cell death (Hetz & Saxena, 2017). In post-mortem examination of MND patients, the ER appears fragmented and distended, with deposits of amorphous material indicating activation of the UPR (Sasaki, 2010).

In the mitochondria, calcium is vital for enzymatic activation in ATP production and mitochondria also serve roles in regulating cytosolic calcium. Under physiological conditions increases in energy demands increase intracellular calcium, which then increases ATP production to meet this demand (Griffiths & Rutter, 2009). However, during pathological calcium influx, mitochondria lose their buffering capacity, and the excess calcium disturbs oxidative phosphorylation. This in turn leads to an increase in the production of reactive oxygen species (ROS), which causes oxidative stress and cell death. Furthermore, excess calcium and ROS production also triggers the opening of the mitochondrial permeability transition pore (mPTP), which leads to mitochondrial swelling and cellular damage (Tadic et al., 2014; Fig. 2).

This calcium-induced mitochondrial dysfunction is known to have a significant role in MND-FTD pathology. Disease-causing mutations in the FUS protein have been shown to disrupt mitochondrial associated membranes in a cell model of MND-FTD, leading to impaired calcium homeostasis and reduced ATP production (Stoica et al., 2016). In a mouse model of disease expressing mutant C9ORF72, mitochondria were entirely malformed, with significant disruptions to the inner mitochondrial membranes. These animals also showed decreased activity in mitochondrial complexes, leading to reduced ATP production (Choi et al., 2019). Mere exposure of rat primary spinal cord cultures to mutant SOD1 generated ROS which led to neuronal death in a matter of days. Subsequently, blocking the mPTP or inhibiting mitochondrial calcium uptake greatly decreased ROS production, preventing neuronal death (Rojas et al., 2015).

These results indicate that vulnerability to calcium excitotoxicity plays a important role in MND-FTD pathology, leading to dysfunctions in the ER mitochondria calcium cycle and subsequent neurodegeneration. While calcium buffering changes are known to exist in the disease state, the functional role of these changes is poorly characterised during normal neuronal spiking activity.

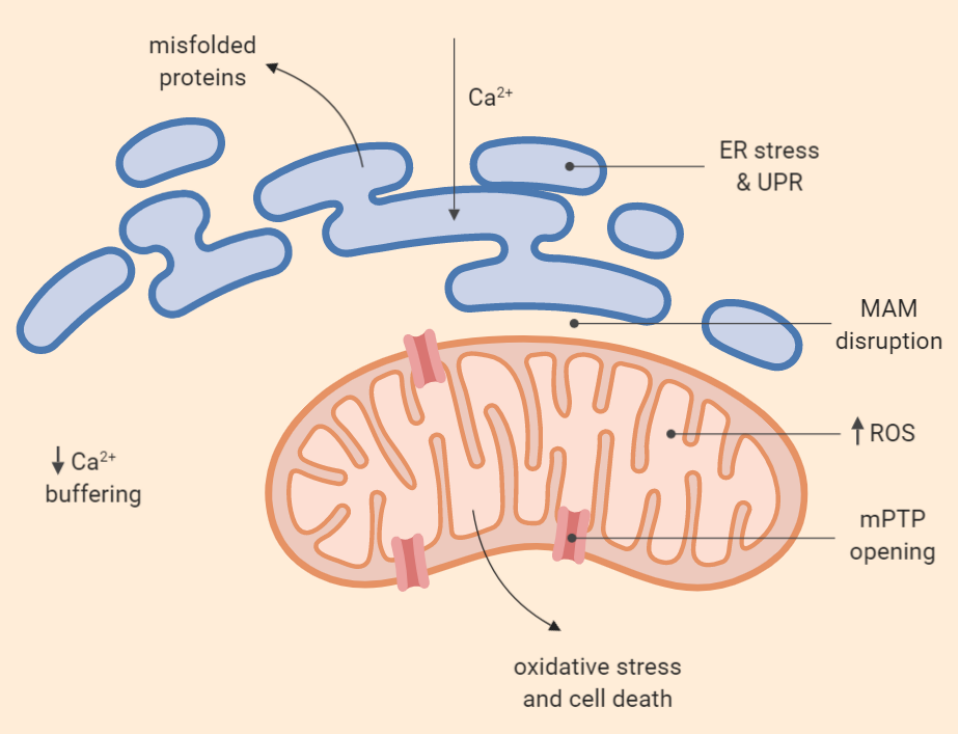

Figure 2: Intracellular calcium dysregulation and disruptions to the ER-mitochondrial calcium cycle in MND/FTD.

Ca^{2+} = calcium, ER = endoplasmic reticulum, UPR = unfolded protein response, MAM = mitochondrial associated membrane, ROS = reactive oxygen species; mPTP = mitochondrial permeability transition pore.

1.5 Excitability changes in MND/FTD

The other essential role played by calcium in the neuron is in action potential initiation, leading to neuronal signalling. Signalling changes have been implicated in disease pathology and appear to change over time with disease progression. However, when comparing evidence from patients and disease models, apparent contradictions begin to emerge. Numerous studies point to hyperexcitability as causative mechanism of neurodegeneration, while other results ostensibly suggest a role for hypoexcitability immediately prior to cell death.

1.5.1 Hyperexcitability in disease

Perhaps the most compelling argument for the hyperexcitability hypothesis in MND/FTD are the transcranial magnetic stimulation (TMS) studies performed in MND. TMS changes are one of the earliest diagnostic criteria available in disease and are in some cases detected even before other clinical symptoms emerge (Menon et al., 2015). Crucially, hyperexcitability in recordings from the motor cortex precedes motor neuron loss in the spinal cord. Moreover, these changes persist across both sporadic and familial patient backgrounds, suggesting that they represent a common disease mechanism. Firstly, TMS reveals that the motor evoked potential (MEP) is significantly increased in MND, where the MEP represents the amplitude response in excitation to a magnetic stimulus. Secondly, the short interval intracortical inhibition (SICI) is also significantly reduced in patients, as defined by the conditioned test stimulus intensity required to stimulate a response following a priming stimulus (Vucic, Nicholson & Kiernan, 2008; Geevasinga et al., 2015).

Other patient data also provides support for hyperexcitability in disease. Widespread fasciculations are observed in disease, arising from the nerve terminals of affected motor neurons indicating changes in neuronal excitability profile (de Carvalho & Swash, 2013). Altered axonal excitability is also present in patients with sporadic disease, arising from a combination of increased sodium influx and potassium channel dysfunction, both indicating hyperexcitability (Kanai et al., 2006). Finally, patients with highly connected brain networks display more rapid disease progression, as measured by structural and functional imaging (Verstraete et al., 2010).

Subsequent studies in cell lines and animal models also confirm this effect. For instance, iPSCs derived from patients harbouring SOD1, C9ORF72, or FUS mutations show hyperexcitability in multielectrode recordings (Wainger et al., 2014). Furthermore, whole-cell patch-clamp recordings from a SOD1 model of MND also demonstrate hyperexcitability in hypoglossal

motor neurons, with concurrent increased spontaneous neurotransmission. Remarkably, these results are evident in neonatal animals from postnatal day four, several months before neurodegeneration and behavioural deficits occur (Van Zundert et al., 2008). Together, the data suggest that brain connectivity and neuronal excitability play a key role in disease.

1.5.2 Hypoexcitability in disease

Still other studies, however, suggest that hypoexcitability plays a key role in diseased neurons. Contrary to the work from Wainger and colleagues which implicated hyperexcitability in patient-derived iPSCs (2014), a group from the Cedars-Sinai Medical Center found that neuronal cultures derived from patients with the C9ORF72 mutation were less excitable than control-derived iPSCs (Sareen et al., 2013). In a more recent iPSC model expressing TDP-43 or C9ORF72 mutations, these two results were perhaps reconciled as temporal differences in excitability. When patient-derived cells matured, they were initially more excitable with significantly more frequent action potentials in response to an electrical stimulus. However, after several weeks, the percentage of patient-derived neurons able to respond to such stimuli decreased significantly (Devlin et al., 2015).

When looking at animal models of disease, there are several models that support the hypoexcitability hypothesis. In a SOD1 mouse model, rather than being hyperexcitable, a fraction of spinal motor neurons instead became unable to maintain firing in response to current ramps (Delestrée et al., 2014). Another mouse model produced similar results with more nuanced excitability changes than outright excitability (Bories et al., 2007). Finally, a recent study of SOD1 and FUS mice examined the large fast-twitch motor units which are selectively vulnerable in disease. These neurons showed a slight increase in response to an initial stimulus but were unable to produce sustained firing beyond an initial response.

Together, these studies report complex excitability changes in patient studies, as well as in animal and iPSC models. In some cases, there is increased sensitivity to input signals, while in others a loss of repetitive firing and reduction in stimulus response is observed prior to cell death. These contradictory results may arise from a fundamental limitation in disease models or may indicate more complex pathomechanisms at work, requiring closer investigation. Virtually all excitability studies in these models leverage electrophysiological techniques, however these techniques are largely designed to measure response to external stimuli. Therefore, a baseline readout of physiological function would be desirable to understand which mechanism dominates in disease pathophysiology.

1.6 Aims and rationale

The aim of this study was to further investigate calcium changes during neuronal signalling and reconcile the evidence for excitability in disease. This project was divided into two parts as follows:

Aim 1: Establish an *in vitro* model of calcium signalling in MND/FTD

Firstly, this study established a method to investigate intracellular calcium changes *in vitro* using primary hippocampal neuronal cultures. Expression of TDP-43 WT, ΔNLS, and A315T variants were transduced in primary neuronal cultures using adeno-associated viruses (AAVs) to model disease state. To track calcium changes, neurons were co-transduced with the genetically encoded jGCaMP7f calcium reporter, which is designed to track calcium dynamics in large neuronal populations as well as at a subcellular resolution (Dana et al., 2018).

Aim 2: Establish an *in vivo* model of calcium signalling in MND/FTD

Subsequently, this study established an *in vivo* model of MND-FTD, by transducing jGCaMP7f into iTDP-43^{A315T} mice, and recording using an integrated miniaturised microscope system. The miniaturised microscope (Miniscope) used in this project is an open source wide-field fluorescent microscope, designed for live recording neuronal activity of freely behaving animals (Cai et al., 2016). These were analysed using new and existing analysis pipelines to determine calcium dynamics and excitability changes in MND/FTD.

2 Methods

2.1 Adeno-associated virus (AAV) constructs

2.1.1 List of constructs

pGP-AAV-syn-jGCaMP7f-WPRE (jGCaMP7f) was a gift from Douglas Kim & GENIE Project (Addgene plasmid #104488). pAAV-CAG-mRuby2 (mRuby2) was a gift from Viviana Gradinaru (Addgene plasmid #99123). pAAV-hSyn-TDP-43-myc variants were previously produced by the Dementia Research Centre (DRC, Macquarie University) by cloning TDP-43 variants into Addgene plasmid #50465 (pAAV-hSyn-EGFP). These variants were full length TDP-43, TDP-43 harbouring the A315T pathological familial mutation, and TDP-43 with truncation of the nuclear localisation sequence (ΔNLS). pAAV-hSyn-TDP-43-mRuby2 variants were then produced by cloning mRuby2 into pAAV-hSyn-TDP-43-myc variants (Table 3; Supp. 1).

Table 3: pAAV constructs and descriptions

Name	Description
pGP-AAV-syn-jGCaMP7f-WPRE	jGCaMP7f calcium sensor (#104488)
pAAV hSyn -TDP43-WT-myc	myc-tagged full length human TDP-43
pAAV hSyn -TDP43-A315T-myc	myc-tagged TDP-43 harbouring pathological A315T mutation
pAAV hSyn -TDP43-NLS-myc	myc-tagged TDP-43 with truncated nuclear localisation sequence
pAAV hSyn -TDP43-WT-mRuby2	mRuby2-tagged Full length human TDP-43
pAAV hSyn -TDP43-A315T-mRuby2	mRuby2-tagged TDP-43 harbouring pathological A315T mutation
pAAV hSyn -TDP43-NLS-mRuby2	mRuby2-tagged TDP-43 with truncated nuclear localisation sequence
pAAV CAG-mRuby2	mRuby2 control (#99123)

2.1.2 TDP-43 mRuby2 variant cloning and validation

TDP-43 mRuby2-tagged variants were produced with help from Mr Mehul Gajwani (DRC, Macquarie University). The mRuby2 fragment was excised from pAAV-CAG-mRuby2 by PCR using the primers 5'- GGGGATATCTTCGAAATGGTGAGCAAGGGAGAGGAAC-3' and 5'- CCCAAGCTTCTACTATTTGTACAGCTCATCCATTCCTC-3'. The PCR product and all TDP-43 backbones were then digested with *Eco*RV and *Hind*III and ligated with T4 DNA ligase (New England BioLabs (NEB), USA) as per the manufacturer's instructions.

Following bacterial transformation, colonies containing the mRuby2 insert were identified by colony PCR using the above primers (Supp. 2a, b), and sequenced with Sanger sequencing (Macrogen, South Korea, Supp. 2c), using the primers 5'-CAGCAATTGGTTGGGGATC-3' and 5'-CCACATAGCGTAAAAGGAGC-3'.

After sequencing, TDP-43 mRuby2 tagged variants were validated by polyethylenimine (PEI) transfection into mouse Neuro-2a (N2a) cells. 0.8 million N2a cells were seeded in 3mL DMEM media, supplemented with 2mM L-glutamine, 1mM sodium pyruvate, 1x penicillin/ streptomycin, and 10% heat-inactivated fetal bovine serum (FBS). The following day, cells were transfected with 0.5µg DNA and 15µg PEI in 1mL 0.9% NaCl. After five days, cultured cells were scraped in 200µL modified RIPA buffer containing 0.1% SDS, 1% NP40, 0.5% sodium deoxycholate, 5mM EDTA, 150mM NaCl, 50mM Tris-HCl (pH 8.0), 30mM NaF, 60mM β-Glycerophosphate, 20mM sodium pyrophosphate, 1mM sodium orthovanadate, and cOmplete™ Mini EDTA-free Protease Inhibitor (11836170001, Roche, Switzerland).

2.1.3 Western blot

Protein concentration of cell lysates was determined using the Bradford assay (BioRad) and 10-20µg of protein was resolved on a 10% SDS-PAGE gel. After separation, proteins were semi-dry transferred onto nitrocellulose membranes (Amersham Protran, GE Healthcare, USA). Blots were blocked in 3% bovine serum albumin (BSA; A9647, Invitrogen, Australia), and probed with antibodies against pan TDP-43 (1:2000, 10782-2-AP, Proteintech, USA), human-specific TDP-43 (1:2000, 60019-2-Ig, Proteintech), GFP (1:2000, ab290, Abcam, UK), and GAPDH (1:5000, MAB374, Merck-Millipore, USA). Blots were then incubated with HRP-conjugated secondary antibodies, visualised using Luminata Crescendo Western HRP Substrate (Millipore) and detected with the ChemiDoc MP System (BioRad).

2.1.4 AAV production

All pAAV constructs were produced in AAV-PHP.B capsids by Ms Yijun Lin of the Dementia Research Centre Viral Core (DRC, Macquarie University). For each pAAV construct, HEK293T cells underwent triple transient transfection with the pAAV plasmid, AAV-PHP.B Rep-Cap plasmid, and pHelper plasmid. Cells were then harvested, and AAV-PHP.B virus was purified and titrated. Viruses will be hereafter referred to as in Table 4, with TDP-43 variants collectively referred to as AAV PHP.B TDP-43 myc- or mRuby2-tagged variants for brevity.

Table 4: pAAV plasmids and AAV PHP.B constructs.

Plasmid name	Virus name
pGP-AAV-syn-jGCaMP7f-WPRE	AAV PHP.B jGCaMP7f
pAAV hSyn -TDP43-WT-myc	AAV PHP.B TDP43-WT-myc
pAAV hSyn -TDP43-A315T-myc	AAV PHP.B TDP43-A315T-myc
pAAV hSyn -TDP43-NLS-myc	AAV PHP.B TDP43-NLS-myc
pAAV hSyn -TDP43-WT-mRuby2	AAV PHP.B TDP43-WT-mRuby2
pAAV hSyn -TDP43-A315T-mRuby2	AAV PHP.B TDP43-A315T-mRuby2
pAAV hSyn -TDP43-NLS-mRuby2	AAV PHP.B TDP43-NLS-mRuby2
pAAV CAG-mRuby2	AAV PHP.B mRuby2

2.2 Primary neuronal culture

Primary hippocampal neurons were provided by the Neuronal Culture Core Facility (NCCF, Macquarie University) as previously described (Fath et al., 2008). Briefly, the hippocampi of E16.5 mouse embryos were sub-dissected and trypsinised. For live-cell imaging and immunocytochemistry, 70,000 hippocampal cells were plated on 12mm glass coverslips coated with poly-D-lysine at 0.1mg/mL in borate buffer. For western blot, 1.5 million cortical cells were plated on 6cm dishes. After two hours incubation in DMEM containing 10% fetal bovine serum, medium was changed, and cells were subsequently maintained in Neurobasal medium containing 2% B27 Supplement and 0.25% Glutamax (Gibco, USA).

2.2.1 Viral transduction and live-cell imaging

At three days in vitro (3 DIV) AAVs were diluted in conditioned Neurobasal medium and applied to neurons for viral transduction of AAV-PHP.B jGCaMP7f, TDP-43 and mRuby2. Neurons were incubated for a further 5 days to allow viral expression.

At 12 DIV, neurons on 6cm dishes were scraped in 200µL RIPA buffer with protease inhibitor and sonicated. Lysates were resolved on an SDS-PAGE gel as above to measure protein expression levels. Starting from 12 DIV, neurons on 12mm coverslips were recorded for 5 minutes every two days using the AxioObserver 7 (Carl Zeiss, Germany) at 5x magnification.

2.2.2 Immunocytochemistry

Following live-cell imaging, neurons were fixed in 4% paraformaldehyde (PFA) and stored in phosphate buffered saline (PBS). For immunocytochemistry (ICC), coverslips were incubated with 0.2% NP40 in PBS for membrane permeabilisation, washed with PBS, and blocked with goat blocking buffer (3% normal goat serum (G9023, Sigma-Aldrich), 2% BSA in PBS) at room temperature for an hour. Neurons were then incubated overnight at 4°C with primary

antibody diluted in blocking buffer. Antibodies were used at the following dilutions; myc (1:500, R950-25, Invitrogen), pan TDP-43 (1:400, 10782-2-AP, Proteintech), and GFP (1:1000, ab290, Abcam). After washing with PBS, neurons were then incubated with Alexa-fluor-488 or -555 conjugated secondary antibodies (1:250, Invitrogen), Alexa-fluor-647 conjugated anti-NeuN (1:250, ab190565, Abcam) and counterstained with 4',6-diamidino-2-phenylindole (DAPI, Molecular Probes), for an hour at room temperature. Coverslips were washed and mounted onto glass slides with Fluoromount-G (Thermo Fisher, USA).

Mounted coverslips were imaged using the AxioScan Z1 (Carl Zeiss) with the included Zen 2.6 (blue edition) software. Individual neurons were imaged using the Olympus BX51 with DP80 camera and CellSens software (Olympus, Japan).

2.3 Mice

C57/BL6 mice were used in the viral dilution study, and during the Miniscope surgical optimisation process. The mThy1.2-TA(41)/pTRE-TDP-43^{A315T}(6) mouse line characterised in the Miniscope study was previously published and subsequently maintained by the DRC. Founder animals for the mThy1.2-tTA line were produced by pronuclear injection of cDNA containing the tTA2 transactivator under the mThy1.2 neuronal promoter onto a C57Bl/6 background. Founder animals for the pTRE-TDP-43^{A315T} line were similarly produced by pronuclear injection of human TDP-43 harbouring the A315T mutation under the pTRE tight promoter.

Male double transgenic mThy1.2-TA(41)/pTRE-TDP-43^{A315T}(6) mice were compared to littermate control mice. All surgical procedures commenced at 2 months of age. Mice were housed on a 12-hour light/dark cycle with ad libitum access to water and chow (SF11-059; Specialty Feeds, Australia).

2.4 Miniscope overview

The Miniscope as described by Cai et al. (2016) was provided by LabMaker (LabMaker UG, Germany). Additional GRIN lenses were provided by Edmund Optics (#64-519, Singapore). Miniscope function was confirmed by comparison with the Olympus BX51 and CellSens software. Here a workflow for Miniscope imaging was established as follows, according to the original Miniscope paper and associated wiki (Cai et al., 2016; UCLA).

2.4.1 Virus dilution study

Mice were anaesthetised with ketamine/xylazine, and Viscotears liquid eye gel (Novartis, Switzerland) was applied. Mice were then shaved, and their skull was cleaned with alternating washes of 70% ethanol and betadine. A sagittal incision was made in the scalp, approximately 0.7mm long, and mice were fixed in a robotic stereotaxic frame (Neurostar, Germany). All coordinates provided are for an adult mouse, which the Neurostar software scaled linearly relative to the mouse skull size. The skull was cleaned, and a small burr hole was drilled into the skull at (-2.1AP, +1.7ML). Using a NanoFil syringe with 34G bevelled needle (World Precision Instruments (WPI), USA), 1µL of AAV-PHP.B jGCaMP7f was injected into the brain at (-2.1AP, +1.7ML, -1.7DV) at varying titres at a rate of 0.3µL/min. After 5 minutes the needle was slowly removed, and the skin closed with surgical staples.

After surgery, mice were administered post-operative buprenorphine and returned to their cages, where they were given HydroGel and DietGel (ClearH_2O, USA), until they had completely recovered, at which point they were returned to a water and chow diet. Mice were monitored daily for seven days following surgery, after which they were monitored twice weekly. Mice were maintained for three weeks after surgery to allow time for viral expression, and subsequently transcardially perfused for tissue analysis.

2.4.2 Viral transduction and lens implantation

At two months of age, mice were prepared for surgery as above. Instead of a sagittal incision, a circular piece of the scalp around 0.7mm in diameter was removed before mice were fixed in the stereotaxic frame. The skull was cleaned of connective tissue, and superficial layers of neck muscle connected to the skull were detached. The skull was scored, and a self-tapping bone screw (19010-00, Fine Science Tools (FST), USA) was placed anterolaterally to bregma, to aid in dental cement adhesion.

A 1.8mm diameter craniotomy was made with a trephine drill bit (18004-18, FST), centred on (-2.1AP, +2.1ML), and the skull fragment carefully removed. 500nL of AAV-PHP.B jGCaMP7f at a titre of $1x10^{14}$ was injected into the brain at (-2.1AP, +1.7ML, -2.0DV) at a rate of 0.3µL/min. After 5 minutes, the syringe was withdrawn 0.3mm to (-2.1AP, +1.7ML, -1.7DV), and another 500nL of jGCaMP7f was injected. After a further 5 minutes wait, the syringe was slowly removed at a rate of 0.1mm/sec.

The GRIN lens was lowered to (-2.1AP, +2.1ML, -1.7DV) at a rate of 1.0mm/min, without tissue aspiration. The lens was then affixed in place using cyanoacrylate glue, and the entire

exposed surface of the skull was covered with dental cement (Ortho-Jet, Lang Dental, USA). Finally, the protruding lens was covered with a protective layer of Kwik-Cast sealant (WPI). Post-surgical care was administered as in the virus dilution study (Fig. 3).

2.4.3 Baseplating and recording

Following lens implantation, mice were given three weeks recovery time to allow the inflammation to subside, and to allow time for jGCaMP7f expression. After this time, mice were again anaesthetised and fixed in the stereotaxic frame. The Kwik-Sil silicone cap was removed, and the GRIN lens carefully cleaned with acetone. The baseplate was attached magnetically to the Miniscope, which was connected to the data acquisition board (DAQ) and computer running the Miniscope Controller software (UCLA Miniscope, https://github.com/daharoni/Miniscope_DAQ_Software). The Miniscope was rotated to find a field of view (FOV) containing clearly visible neurons, together with blood vessels to aid in later motion correction. The scope was removed, and further Ortho-jet dental cement was applied in a semicircular ring around the GRIN lens. The Miniscope was then held in the orientation that the optimal FOV was identified in until the cement had set, and the Miniscope was then removed from the baseplate attachment (Fig. 4).

Every day for the week following baseplating, mice were acclimated to handling and experimenters. Firstly, mice were handled until the protective cap could be easily placed and removed, with minimal resistance from the animal. Mice were then habituated to the Miniscope itself, wearing the scope for ten minutes a day. After acclimation, the Miniscope was attached and mice were imaged for seven minutes in their home cage.

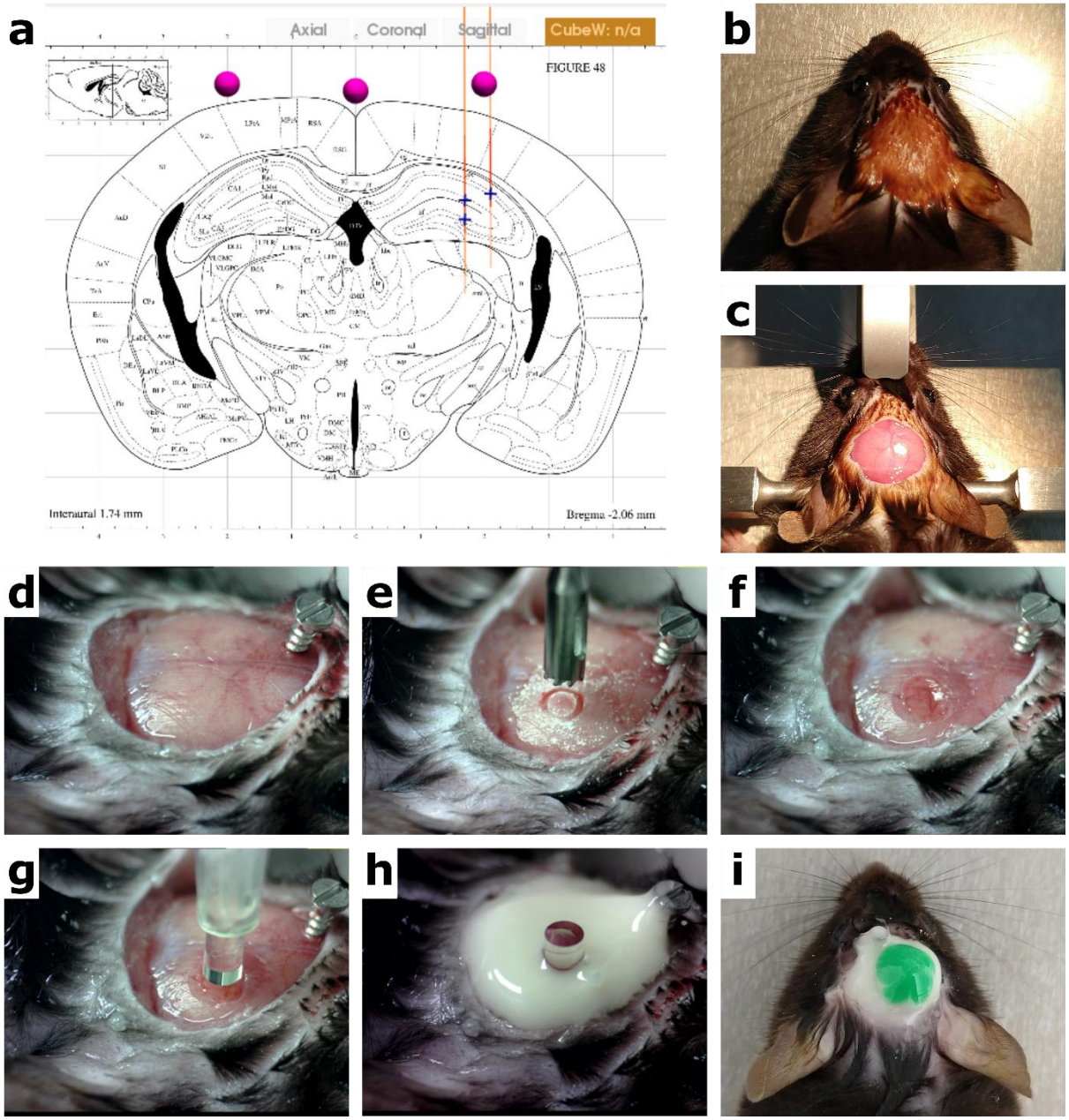

Figure 3: Overview of viral transduction and lens implantation surgery. **a.** Planned injection (*blue crosses, left*) and implantation sites (*blue cross, right*) as per NeuroStar atlas. **b.** The mouse scalp, shaved and prepared for surgery. **c.** The mouse as stabilised in the stereotaxic frame, with open scalp window. **d.** The skull with all connective tissue removed and skull screw implanted anterolateral to bregma. **e.** 1.8mm craniotomy as drilled by trephine drill bit. **f.** Cranial window cleaned of bone fragments and dura, revealing brain tissue. **g.** The GRIN lens is centred over the craniotomy in lens holder, and slowly lowered into place. **h.** The lens in secured with cyanoacrylate glue and dental cement, covering all exposed skull and the skull screw. **i.** The mouse is removed from the frame, and exposed lens is covered by Kwik-Sil silicone.

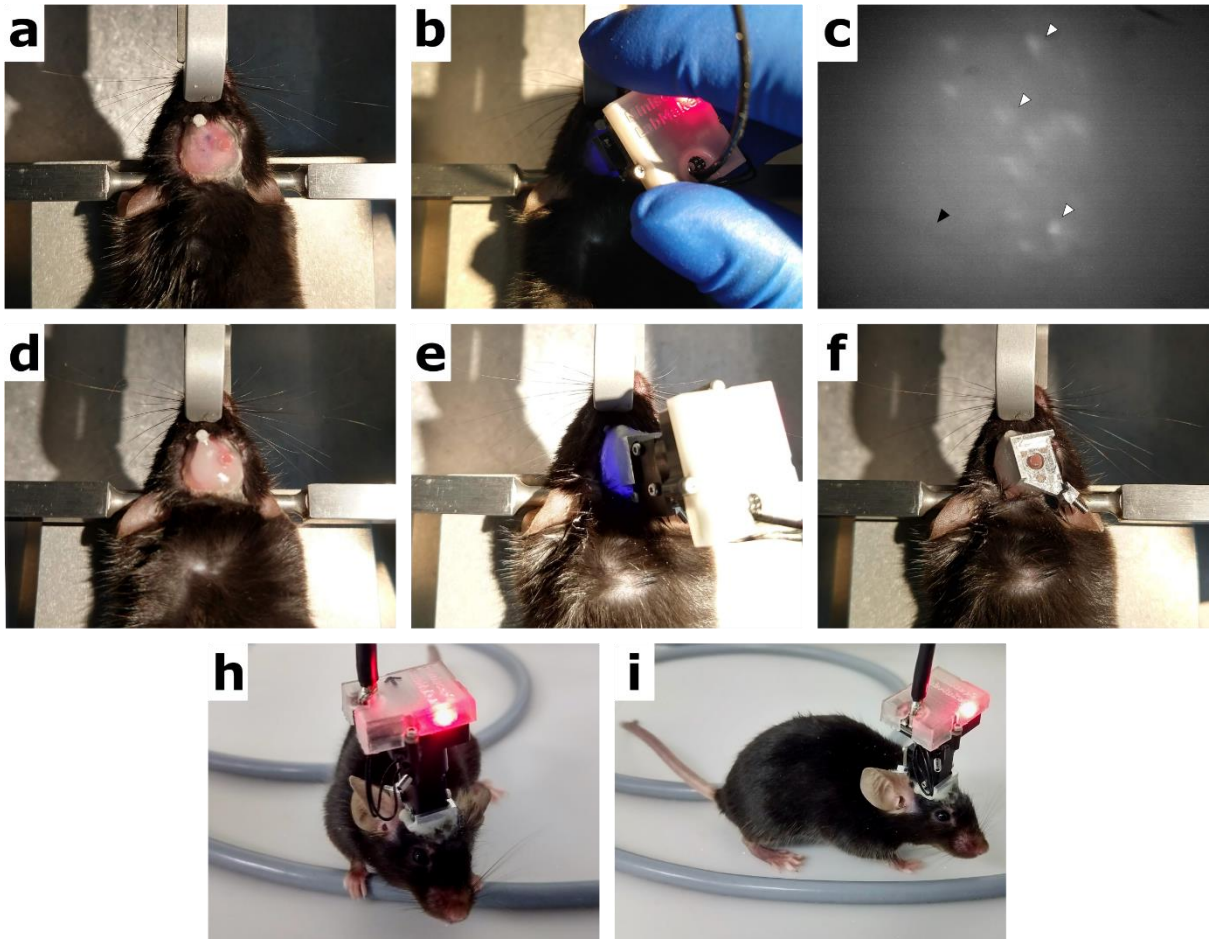

Figure 4: Overview of baseplating procedure. **a.** The mouse stabilised in the stereotaxic frame, with protective silicone removed. **b.** The Miniscope as rotated, and the focus slider adjusted to identify a field of view **c.** containing clearly visible neurons (*white arrowheads*) and blood vessels (*black arrowhead*). **d.** Dental cement was applied around the GRIN lens. **e.** The Miniscope cemented over the identified field of view. **f.** The baseplate located correctly over the lens, with Miniscope removed. **h.** & **i.** The animal recovered from surgery, ready for recording.

2.4.4 Histology

After the virus dilution study or on completion of Miniscope imaging, animals were administered anaesthetic and transcardially perfused with PBS. Brains were removed and postfixed for 24 hours in 4% PFA, before being transferred to PBS.

Brains were then divided coronally at the injection site, for animals that underwent the virus dilution study, or the centre of the lens implant tract, for animals which underwent the Miniscope procedure. Both halves of the brain were embedded in a 2% agarose gel made with PBS and coronally sectioned into 50µm sections using a 7000smz-2 vibrating microtome (Campden Instruments Ltd., England). Sections were mounted onto Superfrost glass slides, and coverslipped with Fluoromount-G. Slides were then imaged using the AxioScan Z1 with Zen 2.6 (blue edition) software. Individual neurons were imaged with the LSM880 confocal microscope with Zen 2.3 (black edition) software (Carl Zeiss).

2.5 Analysis

2.5.1 Image analysis

Live cell recordings were analysed using the FIJI distribution of ImageJ (Schindelin et al., 2012), and the FluoroSNNAP MATLAB software package published and maintained by the Molecular Neuroengineering Lab at the University of Pennsylvania (Patel et al., 2015). For each live cell recording, a video stack of a synchronous calcium event was extracted to measure peak amplitude. In FIJI, the maximal fluorescence was taken across the whole stack. The background was then corrected by subtracting a frame taken immediately prior to initiation of the action potential, with no visible calcium transients, from the peak amplitude stack. From this image, the average corrected total cell fluorescence (CTCF) was generated. CTCF was calculated as the total cell fluorescence visible in frame, less residual background, divided by the number of neuronal bodies visible. Using the FluoroSNNAP toolkit semi-automated segmentation was then performed to identify regions of interest (ROIs), from which fluorescence over time was extracted and normalised to a $\Delta F/F$ trace. From these fluorescence traces, calcium events were identified by template-based detection, and single cell calcium dynamics were recorded.

Miniscope recordings were analysed using the CaImAn Python package published and maintained by the Flatiron Institute (Giovannucci et al., 2019). This package contains a complete analysis pipeline for batch processing large calcium signalling datasets. As a brief overview, source videos were first cleaned of motion artefacts using the NoRMCorre algorithm (Pnevmatikakis & Giovannucci, 2017), source extraction was then performed using the constrained non-negative matrix factorization (CNMF) algorithm (Pnevmatikakis et al., 2016), and individual neurons were deconvolved using the Online Active Set method to Infer Spikes (OASIS) algorithm. Fluorescence traces were then extracted from each neuron for further analysis. A sample of the source code used in this project is available in Supp. 3 with output included. The complete code base is available on request.

2.5.2 Statistical Analysis

Statistical analysis was performed using GraphPad Prism 8.2 software. Live cell results were analysed using two-way ANOVA or mixed-effects analysis, comparing calcium dynamics across TDP-43 variants over time. Grouped comparisons were made to identify the main effect of TDP-43 variant on calcium signalling, with matched values across time points, and the main effect of time on calcium signalling. Results were adjusted for multiple comparisons using Tukey's multiple comparisons test. Live cell recordings were excluded from analysis where a

calcium event could not be identified in the 5-minute recording. One TDP-43-WT-myc, and one TDP-43-A315T-myc transduced well was excluded at 12 DIV; and one jGCaMP7f only well was excluded at 18 DIV. Eight representative neurons were selected from each Miniscope recording and compared using two-tailed Student's t-test.

All values and error bars are presented as the mean and standard error of the mean, and p-values less than 0.05 were considered statistically significant.

3 Results

3.1 *In vitro* experimental **overview**

The first aim of this project was to develop an *in vitro* model system, suitable for investigating the relationship between TDP-43 expression and neuronal excitability. In this system, primary hippocampal neurons were co-transduced with jGCaMP7f and TDP-43 variants via AAV. Single transduction with jGCaMP7f AAV served as control. Cells were given nine days to express viral constructs and imaged every two days thereafter (Fig. 5). Section 3.2 describes the generation, validation, and optimisation of viral constructs for transduction. Section 3.3 then reports on the signalling changes observed in this model.

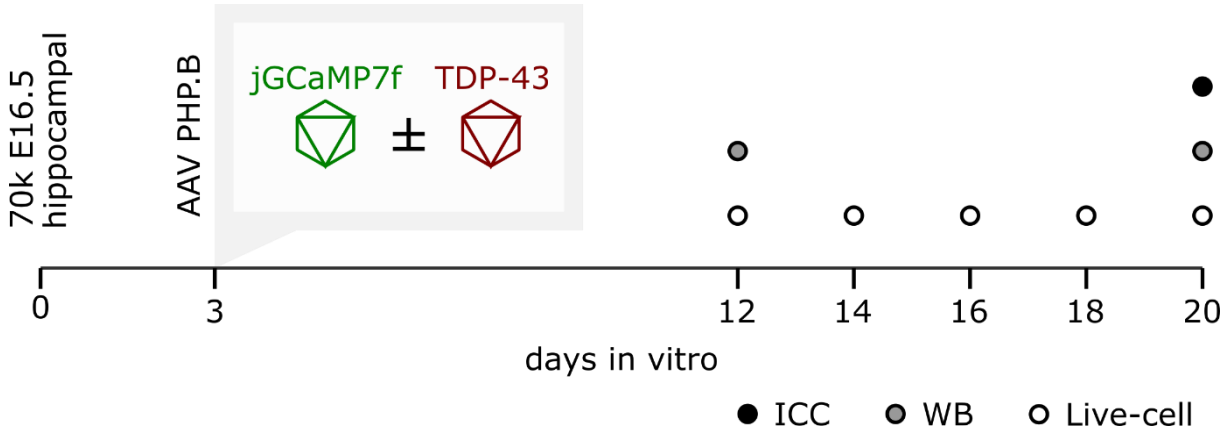

Figure 5: Experimental overview for primary hippocampal cultures. Hippocampal cultures were transduced with AAV PHP.B constructs at 3 DIV and given 9 days to express viral constructs. Cells were then imaged every two days from 9 DIV until 20 DIV, with validation by western blot (12, 20 DIV) and immunocytochemistry (20 DIV). DIV = days *in vitro*.

3.2 Construct validation and *in vitro* optimisation

3.2.1 Validation of TDP-43-mRuby2 variant plasmids

To generate TDP-43-mRuby2 variant plasmids, the myc-tag was excised from pAAV-hSyn-TDP-43-myc (previously generated in the Ke lab) and replaced with the mRuby2 tag amplified from pAAV-CAG-mRuby2 (Section 2.1.2; Supp. 1, 2). After generation of TDP-43-mRuby2 variants, plasmids were validated by PEI transfection into mouse neuroblastoma N2a cells. After 5 days, cells were lysed, and protein levels were measured by Western blot (Fig. 6).

Probing with antibodies against pan-TDP-43 allows for detection of both endogenous mouse TDP-43 and transfected human TDP-43 variants, while probing for human specific TDP-43 isolates transfected TDP-43. When probing for pan-TDP-43, cells transfected with mRuby2 empty vector control showed a band at ~55kDa, indicating glycosylated TDP-43, with faint banding from various other post-translational modifications. Expression was confirmed in cells transfected with hTDP-43-mRuby2 WT, A315T and ΔNLS by the presence of a ~70kDa band due to the fusion of mRuby2 (26.5kDa) as a tag to TDP-43 (43kDa). Probing for hTDP-43 isolated only the larger fusion band in hTDP-43-mRuby2 transfected samples, confirming successful transfection with TDP-43-mRuby2 constructs.

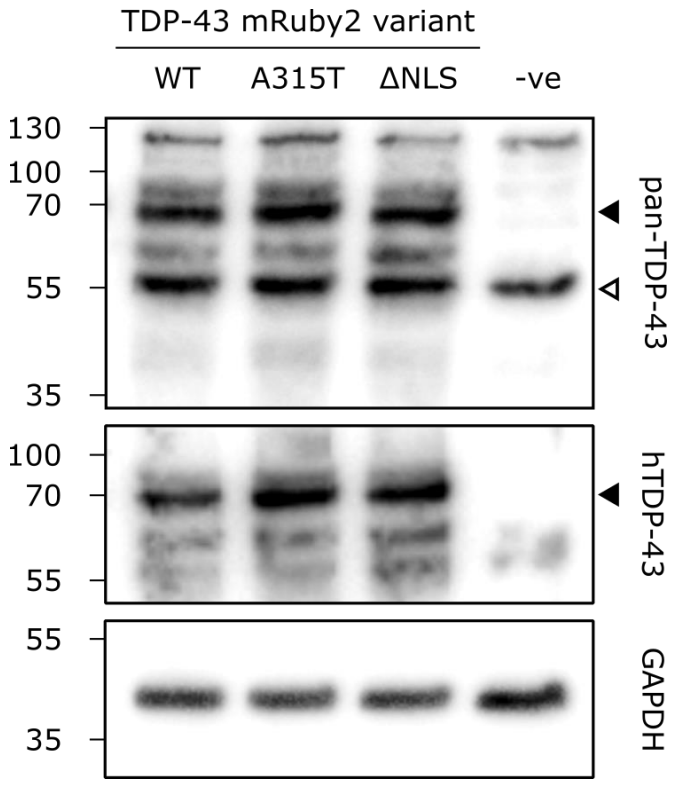

Figure 6: Comparison of protein expression levels in N2a cells transfected with TDP-43 variants (WT, A315T, or ΔNLS) or mRuby2 empty vector control (-ve). *Top:* Probing with antibodies against total TDP-43 (pan-TDP-43), reveals a ~55-kDa band in control cells (*open arrow*), with additional TDP-43-mRuby2 fusion band at ~70kDa in TDP-43-mRuby tagged cells (*closed arrow*). *Middle:* Probing with human specific TDP-43 (hTDP-43) (*closed arrow*) further confirming successful transfection. *Bottom:* GAPDH as loading control.

3.2.2 *In vitro* viral transduction validation and optimisation

jGCaMP7f and TDP-43 variant AAVs were produced as described in Methods section 2.1.4. Single transduction validation of each AAV in primary hippocampal neuronal cells was initially carried out to confirm successful AAV packaging and production. The jGCaMP7f calcium sensor fluoresces upon calcium influx and binding, which indicates neuronal excitation. Increasing titre of AAV PHP.B jGCaMP7f resulted in increasing levels of green fluorescence during spiking activity up to a titre of $1x10^9$ vg/well, which corresponds to a multiplicity of infection (MOI) of $1.5x10^4$. At higher titres, cells experienced neuronal toxicity associated with excessive calcium binding (Fig. 7a).

Viral transduction with AAV PHP.B TDP-43 myc-tagged constructs resulted in similar levels of TDP-43 expression between variants as demonstrated by immunocytochemistry (Fig. 7b). TDP-43-WT and -A315T variants expressed primarily nuclear TDP-43 with diffuse cytoplasmic staining, while ΔNLS variants showed strong cytoplasmic TDP-43 expression.

For live-cell imaging, AAVs with TDP-43 variants mRuby2-tagged were also produced. Primary hippocampal neurons were transduced with TDP-43-mRuby2 AAV variants or mRuby2 control AAV. At 12 DIV, transduced neurons fluoresced brightly when illuminated by an LED emitting 577nm light, with no such fluorescence in matched TDP-43 myc-tagged wells (Fig. 7c). However, TDP-43-mRuby2-transduced neurons experienced rapid cell death after 12 DIV, akin to previous observations in the Ke lab with mCherry-tagged TDP-43 variants. As such, TDP-43 mRuby2-tagged variants were excluded from further study. All subsequent experiments were performed with myc-tagged TDP-43 variants at a titre of $3x10^9$ vg/well.

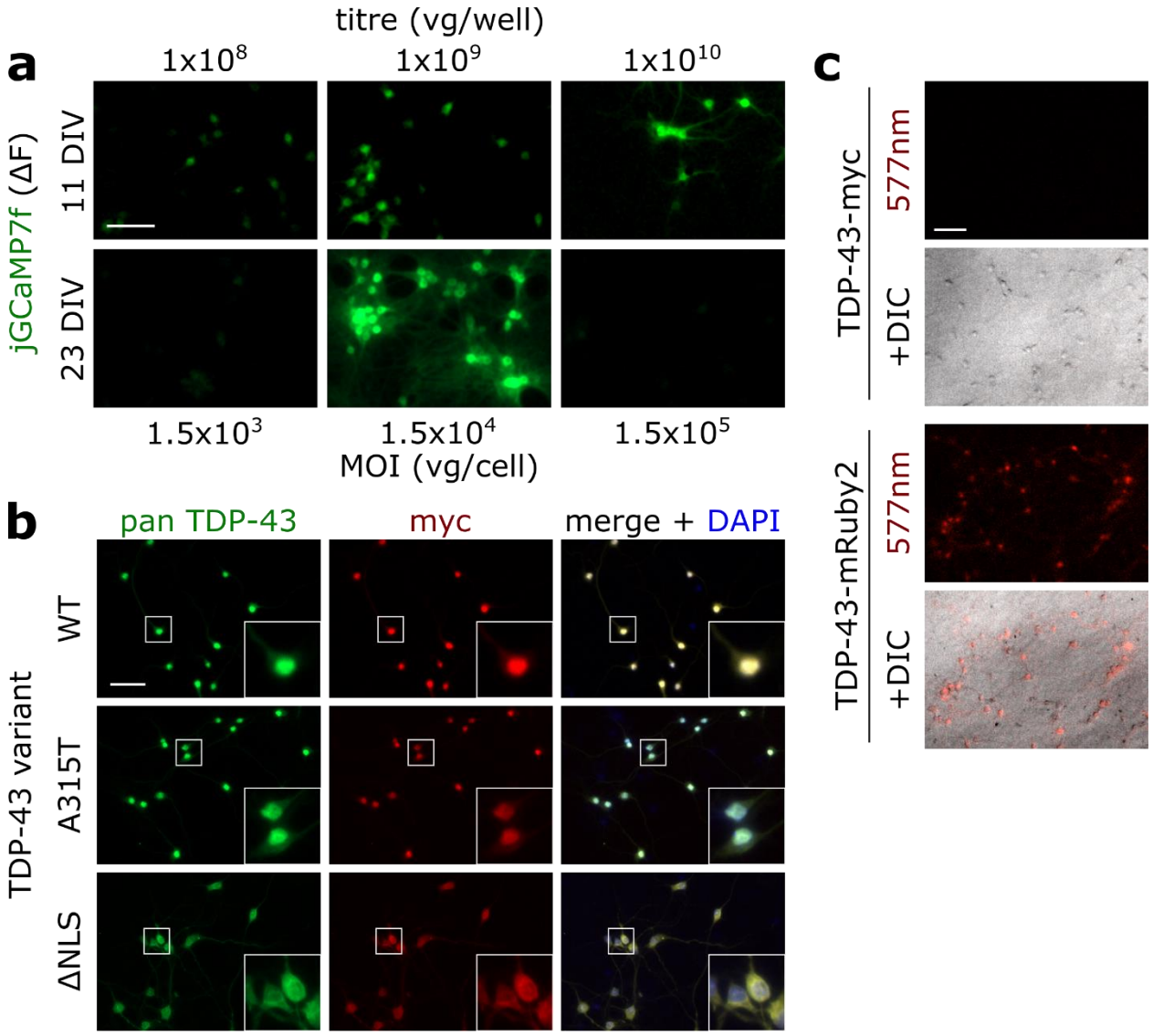

Figure 7: Validation of viral constructs by single transduction. **a.** Representative images of primary hippocampal neurons transduced with AAV PHP.B jGCaMP7f at a titre of $1x10^8$, $1x10^9$ & $1x10^{10}$ vg/well. Cells were imaged at 11 and 23 days *in vitro* (DIV), images show change in fluorescence over background. *Scale bar:* 100µm. **b**. Representative images of primary hippocampal neurons transduced with AAV PHP.B TDP-43 myc-tagged variants at a titre of $3x10^9$ vg/well (MOI 4.5 vg/cell). *Inset:* TDP-43-WT and -A315T variants displayed primarily nuclear TDP-43 expression, while TDP-43-ΔNLS neurons showed nuclear exclusion of TDP-43. *Scale bar:* 50µm. **c.** Representative images of neurons transduced with TDP-43-myc or TDP-43-mRuby2. Across all TDP-43-mRuby2 constructs, neurons fluoresced red indicating successful transduction. *Scale bar:* 100µm.

3.2.3 Co-transduction system validation

Primary hippocampal cultures were co-transduced with AAV PHP.B jGCaMP7f and AAV PHP.B TDP-43-myc variants. To confirm levels of protein expression across conditions, cells were lysed for western blot at 12 and 20 DIV (Fig. 8a). Lysates were probed for pan TDP-43 and human-specific TDP-43 to confirm expression. AAV PHP.B TDP-43-myc transduction resulted in TDP-43 overexpression with all TDP-43 variants. Single-transduced jGCaMP7f control cells showed a single band of endogenous TDP-43 at ~43kDa, while TDP-43-myc co-transduced cells showed several additional bands of hTDP-43-myc and its post-translational forms. As the jGCaMP7f calcium sensor is a GFP-based fusion protein, cell lysates were further probed for GFP to detect jGCaMP7f levels. All transduced cells showed a ~55kDa band, representing the jGCaMP7f fusion protein.

Additionally, at 20 DIV, neurons were stained by immunocytochemistry to confirm expression in all transduced cells (Fig. 8b). jGCaMP7f was present in all coverslips as detected by GFP-positive staining, while only AAV PHP.B TDP-43-myc transduced cells stained positively for myc. Furthermore, all neurons identified by NeuN positive staining expressed jGCaMP7f and myc, except in the case of single-transduced coverslips, indicating successful transduction with the AAV-PHP.B system at the previously determined titres.

Figure 8: In vitro co-transduction validation. **a.** Validation of GCaMP transduction levels by Western blot. ► *Top*: Probing for pan-TDP-43 revealed endogenous TDP-43 (~43kDa), with additional hTDP-43-myc bands in AAV PHP.B TDP-43-myc variant transduced cells. *Middle-upper*: Probing for hTDP-43 isolated transduced TDP-43 in TDP-43 transduced cells. *Middle-lower*: Probing for GFP revealed a jGCaMP7f band (~55kDa) in single-transduced cells, and no change in expression levels over time. Bottom: GAPDH loading control. **b.** Representative ICC images taken of cells transduced with AAV PHP.B jGCaMP7f and TDP-43-myc variants. Cells were immunostained with antibodies against GFP (jGCaMP7f, *green*), myc (TDP-43, *red*), and NeuN (*magenta*), with DAPI counterstain. *Scale bar*: 50µm.

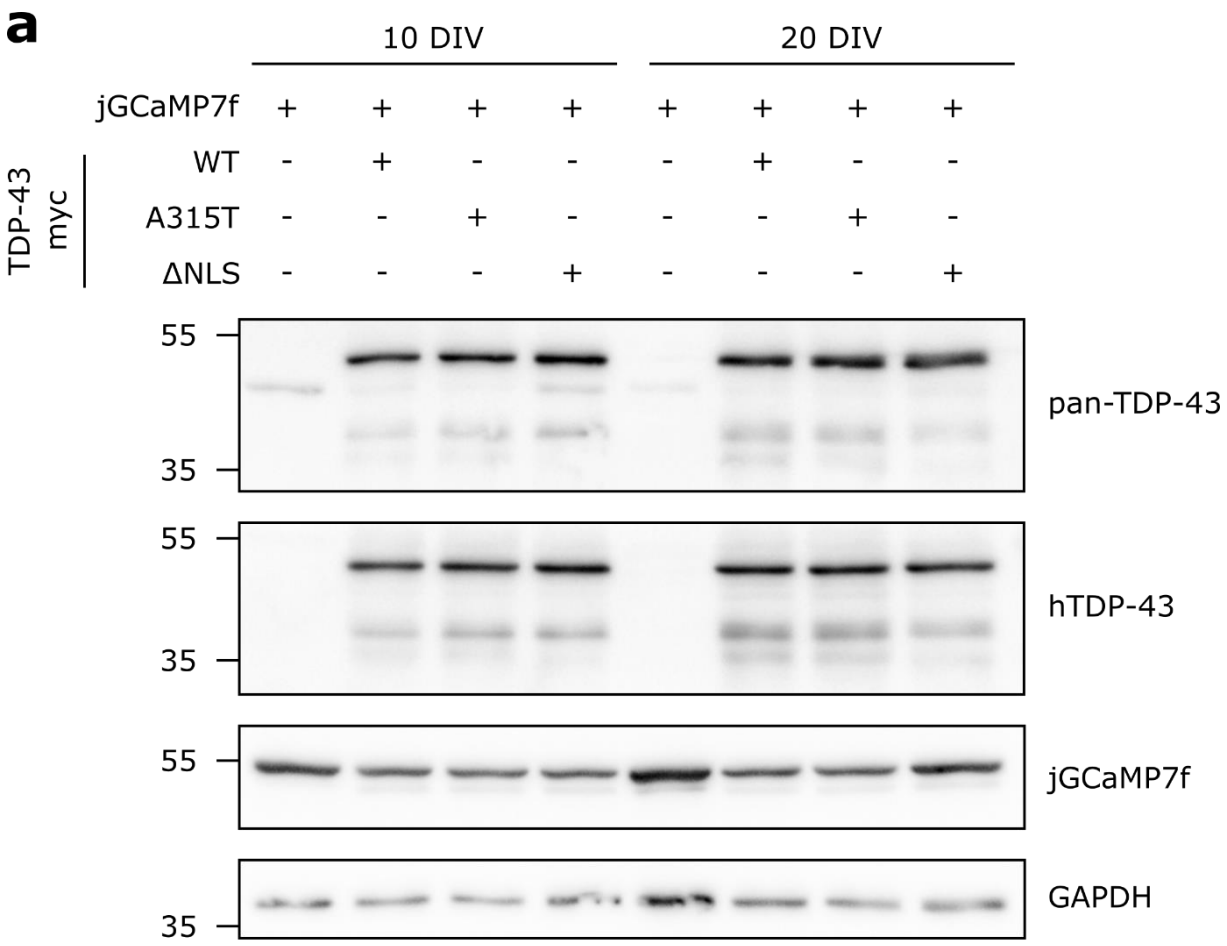
a
10 DIV
20 DIV
jGCaMP7f + + + + + + + +
TDP-43 myc
WT - + - - - + - -
A315T - - + - - - + -
ΔNLS - - - + - - - +
55
35
pan-TDP-43
55
35
hTDP-43
55
jGCaMP7f
35
GAPDH

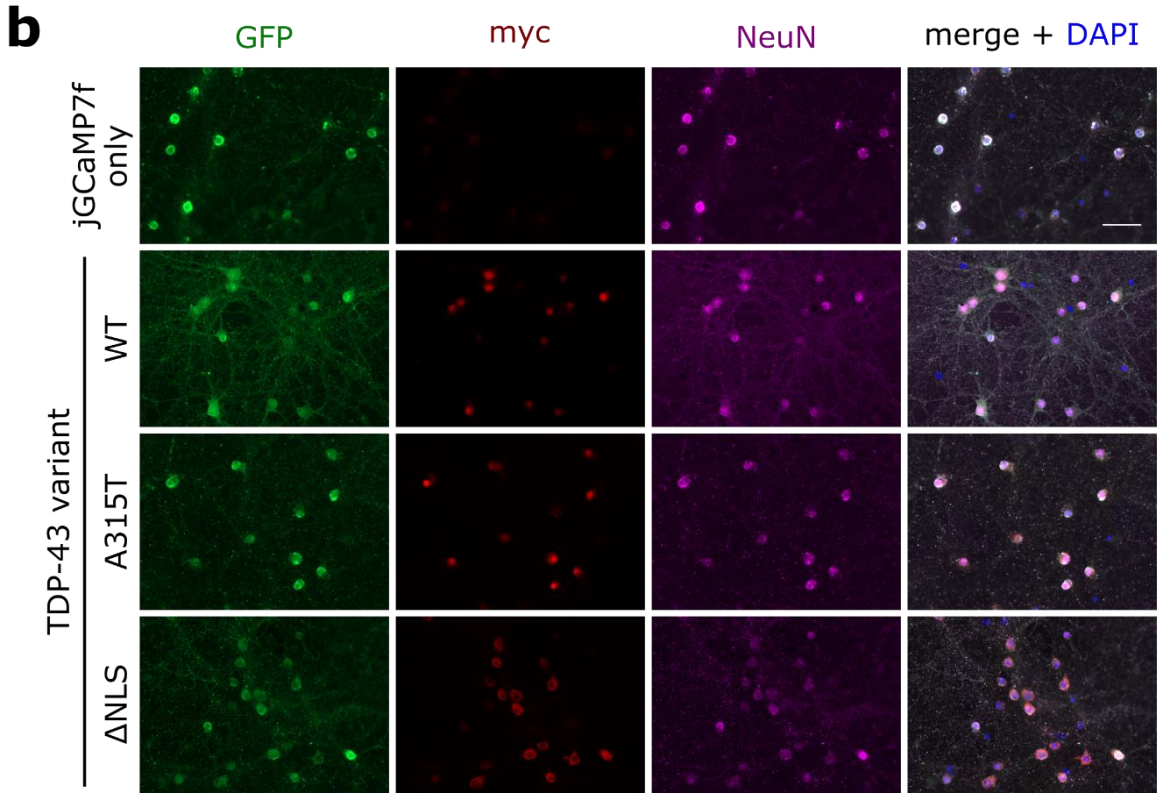
b
GFP
myc
NeuN
merge + DAPI
jGCaMP7f only
TDP-43 variant
WT
A315T
ΔNLS

3.3 TDP-43 expression *in vitro* changes neuronal signalling patterns

3.3.1 TDP-43 overexpression *in vitro* reduces responsiveness to spontaneous activity

Neuronal cultures co-transduced with AAV PHP.B GCaMP7f and TDP-43-myc variants were measured for calcium responsiveness to explore excitability changes. To measure calcium response during spiking activity, peak cell fluorescence was measured in primary hippocampal neurons transduced with jGCaMP7f and TDP-43-myc tagged variants at two-day intervals from 12 to 20 DIV. At each time point a synchronous calcium event was identified, where over 90% of neurons in the field of view fired simultaneously. For every such event, the background was subtracted, resulting in corrected total cell fluorescence per cell in relative fluorescence units (rfu).

Neurons that were single transduced with jGCaMP7f showed gradually increasing CTCF over time. This increase was weakly mirrored in TDP-43-WT and -A315T transduced cells. However, calcium influx in TDP-43-ΔNLS transduced cells showed no such increase over time (Fig. 9a). Calcium responsiveness was significantly greater in jGCaMP7f single-transduced neurons than all other groups across all time points (3522±254 rfu at 20 DIV). TDP-43-WT and -A315T transduced cells showed comparable fluorescence during synchronised spiking (1438 ±234 and 1584±34 rfu at 20 DIV). TDP-43-ΔNLS transduced cells showed significantly less fluorescence than all other groups during peak spiking (698±42 rfu at 20 DIV; Fig. 9b). The number of neurons participating in synchronous spiking gradually increased over time, with no significant difference in the number of neuron participation between groups, (Supp. 4).

All TDP-43 transduced neurons experienced reduced calcium binding, with the most pronounced reductions evident in the functional TDP-43-ΔNLS mutant. These results demonstrate that TDP-43 overexpression attenuates neuronal responsiveness to spontaneous electrical activity.

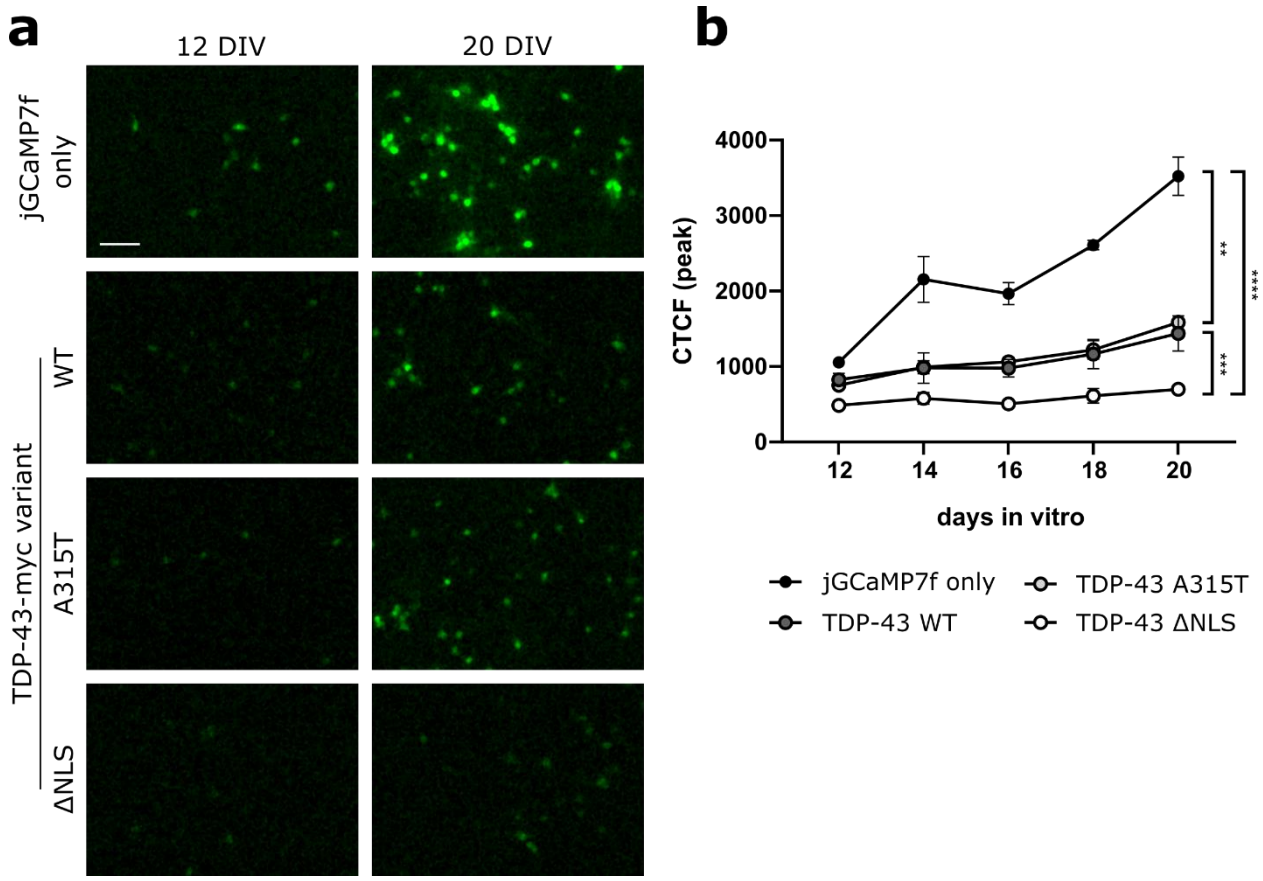

Figure 9: TDP-43 expression reduces calcium response to spontaneous electrical activity. **a.** Representative image of peak jGCaMP7f spiking in TDP-43-WT, -A315T, -ΔNLS and jGCaMP7f only transduced neurons. *Scale bar:* 100µm **b.** Quantification of corrected total cell fluorescence (CTCF) over each synchronous spiking event in relative fluorescence units. Multiple comparisons were made between all groups. No significant difference was observed between TDP-43-WT and -A315T transduced cells. (**, $p < 0.01$; ***, $p < 0.001$; ****, $p < 0.0001$; n = 3 virally transduced wells in technical replicate).

3.3.2 TDP-43 overexpression *in vitro* alters neuronal signalling

The disturbances in intracellular calcium response were predicted to result in modulation of underlying spiking patterns, given the excitability changes previously noted in the literature. Live-cell recordings were therefore scored for calcium signalling events as a functional readout of electrical signalling activity.

Inspecting traces of calcium activity, simultaneous calcium signalling events can be distinguished from spontaneous, asynchronous calcium transients (Fig. 10a). All such synchronous events were identified and scored for neuronal participation and duration. Generally, neuronal participation in synchronous calcium events increased over time. At 12 DIV, events showed 60.38±4.74% neuronal recruitment, which increased to 92.20±3.62% by 20 DIV, with no significant difference in participation rates between groups (Supp. 5).

The duration of synchronous signalling events tended to increase over time in jGCaMP7f single-transduced neurons, where event duration increased from 13.26± 3.40s at 12 DIV to 23.35± 1.26s at 20 DIV. However, this increase in event duration was significantly attenuated in all TDP-43 transduced neuronal cultures. By 20 DIV, TDP-43-WT and -ΔNLS co-transduced neurons were experiencing signalling events that lasted 13.09±1.50s and 11.88±1.18s respectively. TDP-43-A315T co-transduced neurons displayed the shortest event duration, at 8.23± 2.06s by 20 DIV, which was significantly less than jGCaMP7f single-transduced and TDP-43-WT co-transduced groups (Fig. 10b).

Taken together, TDP-43 variant expression reduces calcium response and modulates spiking patterns in neurons. Mutations in TDP-43 further exacerbate these effects with severely attenuated calcium response in the functional TDP-43-ΔNLS mutant, and reduced signalling event duration caused by TDP-43 harbouring the pathological A315T mutation.

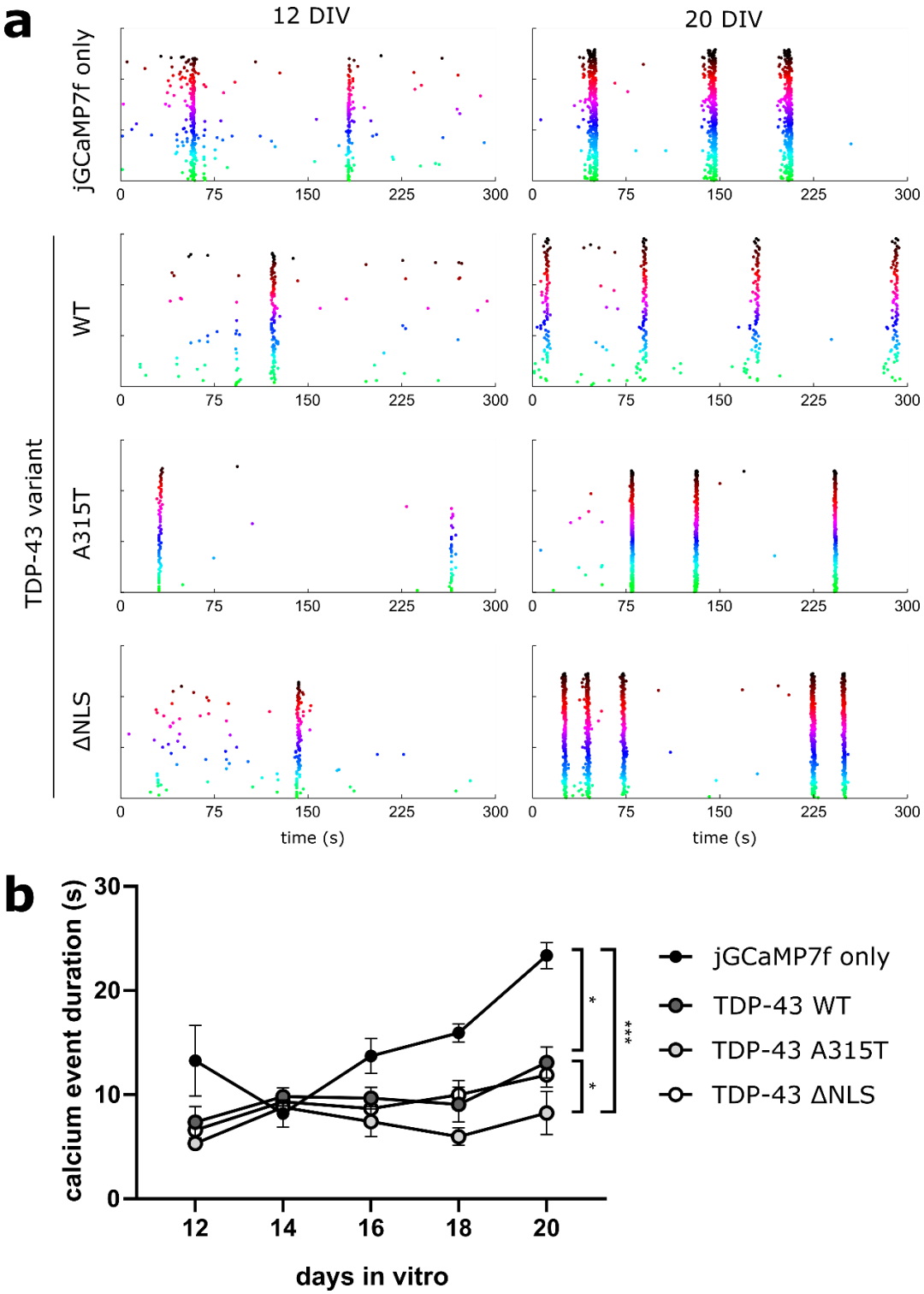

Figure 10: TDP-43 expression alters neuronal spiking patterns. **a**. Representative raster plots of calcium activity in neurons transduced with AAV PHP.B jGCaMP7f or co-transduced with AAV PHP.B jGCaMP7f and TDP-43 variants. Each row across the y-axis represents an individual neuron index, with time (s) across the x-axis. When a neuron fires an action potential, a dot is placed in the corresponding time point. Neurons are grouped according to activity modules and colour coded by FluoroSNNAP (Patel et al., 2015). **b**. Quantification of synchronous signalling event duration in **a**. TDP-43 transduced cells experienced shorter signalling events, with the shortest events in TDP-43-A315T transduced cells. Multiple comparisons were made between all groups. No significant difference was observed between TDP-43-WT and -ΔNLS transduced neurons. (*, $p < 0.05$; ***, $p < 0.001$; $n = 3$ virally transduced wells in technical replicate).

3.4 *In vivo* experimental overview

The second aim of this project was to establish an *in vivo* system for live recording of calcium signalling in our mouse model of MND/FTD. The open-sourced miniaturised microscope (Miniscope) was implanted directly into the cortex of freely-moving iTDP-43^{A315T} MND/FTD mice for live imaging of the calcium sensor jGCaMP7f. Section 3.5 outlines the process of establishing the Miniscope system and provides an overview of the final procedure, acceptance criteria, and the analysis pipeline. Section 3.6 then details the preliminary results achieved using the Miniscope in iTDP-43^{A315T} mice.

3.5 Establishing the Miniscope system

3.5.1 *In vivo* AAV-PHP.B hSyn-jGCaMP7f optimisation

Mice were injected with 1µL AAV-PHP.B hSyn jGCaMP7f at varying titres from 3x10^{12} vg/mL to 1x10^{14} vg/mL to identify the optimal titre for calcium imaging. One month after injection, mice were transcardially perfused and brains were collected from all animals and visually inspected to compare expression levels. jGCaMP7f expression was clearly visible in all samples, having spread throughout the hippocampus on the ipsilateral side of injection. Increasing viral expression was observed with increasing titres across all viral titres used. (Fig. 11a).

Slides were then imaged on the Zeiss LSM880 confocal microscope to observe jGCaMP7f distribution within neurons. The ideal neuron for *in vivo* imaging should express strong cytosolic jGCaMP7f, with nuclear clearance. Neurons transduced with jGCaMP7f exhibited homogenous jGCaMP7f expression at lower titres, with a small degree of nuclear clearance observed at higher titres (Fig. 11b). The AAV titre of 1x10^{14} was selected for subsequent experiments.

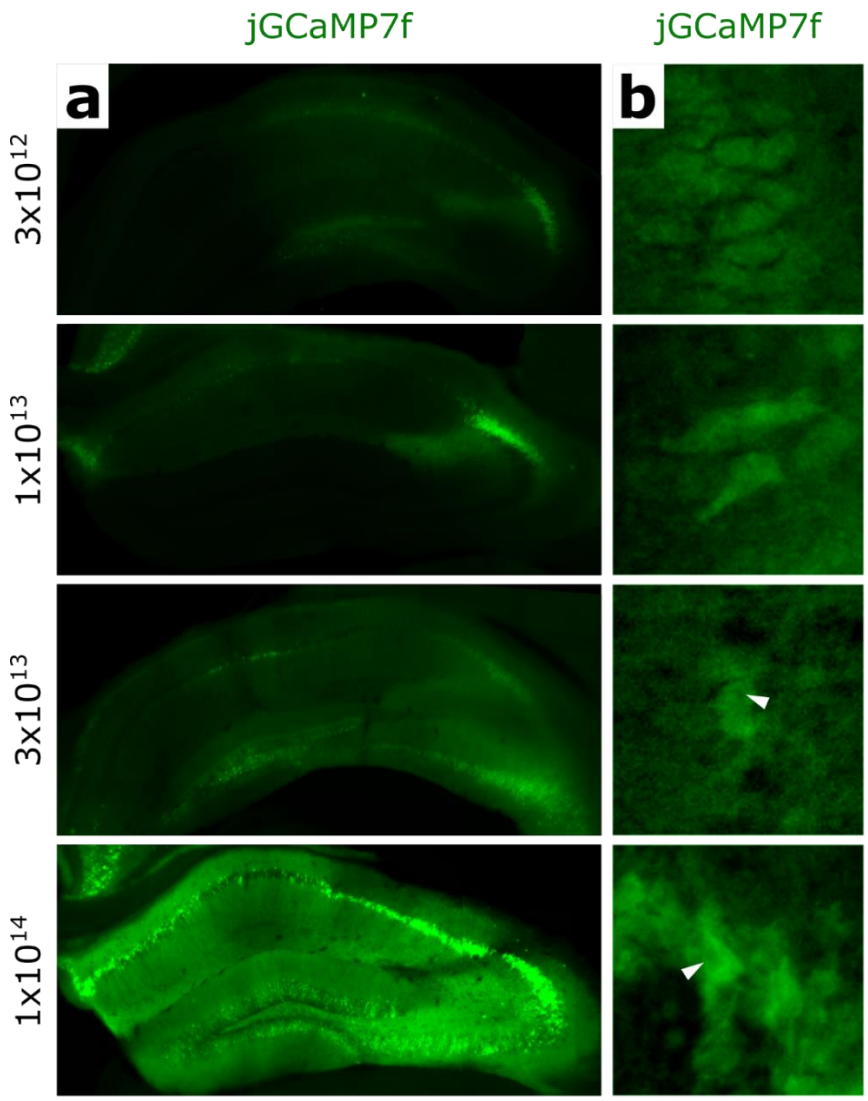

Figure 11: *In vivo* viral transduction optimisation. **a**. Coronal vibratome sections of the whole right hippocampus showing jGCaMP7f expression patterns. jGCaMP7f was clearly visible in all samples, with increasing expression observed with increasing viral titre. **b**. Confocal images taken from the injection site show a small degree of nuclear clearance at higher titres (*arrowheads*).

3.5.2 Initial testing of assembled Miniscope

Excitation light from the blue LED in the Miniscope passes through the lenses and filters of the light path down through the GRIN lens. Emitted light from 2-300µm below the Miniscope is pulled into focus through the GRIN lens and passes up to the CMOS imaging sensor (Fig. 12a). With the present filter set, the Miniscope images light emitted in the 500nm to 550nm range.

To check the functionality of the newly assembled Miniscope, the GRIN lens was internally affixed, and a test slide labelled with Alexa-fluor-488 was imaged (Fig. 12b). The resulting images were comparable in scale to those achieved on a benchtop microscope using a 10x objective (Fig. 12c). This confirmed functionality of the CMOS imaging sensor, and

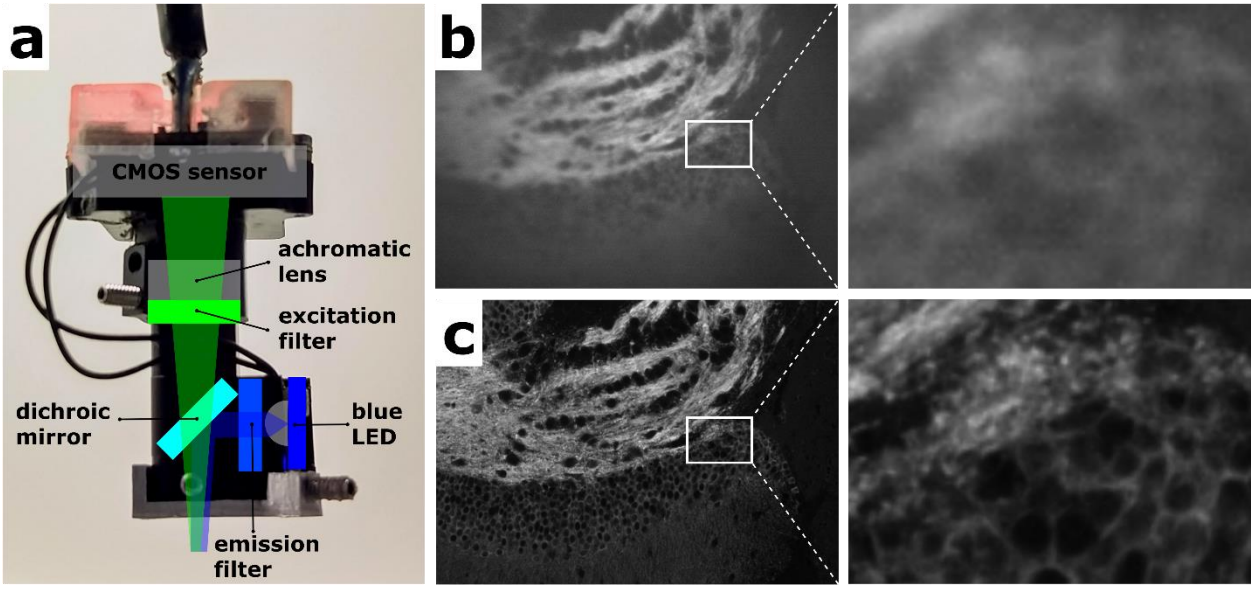

Figure 12: Miniscope structure and initial testing **a.** The assembled Miniscope, with schematic overlay of internal components. Light is emitted from the blue LED, passes through the half ball lens blue emission filter, reflects off the dichroic mirror and passes out through the GRIN lens. **b.** Alexa-fluor-488 immunostained test slide as imaged by the Miniscope. **c.** The above test slide, imaged on the Olympus BX51 tabletop microscope at 10x magnification for comparison.

connections between the scope, data acquisition box, and computer. Correct function of the Miniscope controller software was also established, with the imaging setup able to image comfortably at up to 15 frames per second (FPS) for 7 minutes with no dropped frames.

3.5.3 Miniscope overview and analysis pipeline

The complete Miniscope procedure was established following the guidelines outlined in the original Miniscope paper and associated wiki (Cai et al., 2016; UCLA; Methods 2.4). At two months of age, mice underwent the lens implantation and viral injection surgical procedure (Methods 2.4.2). Mice were given three weeks recovery time, and the baseplate was then attached in the imaging location. After a further week of acclimation and handling, at three months of age, mice were then imaged for seven minutes at 15 FPS (Methods 2.4.3; Fig. 13a). On conclusion of *in vivo* imaging all brains were coronally sectioned to confirm viral injection and correct lens implantation into the CA1 target site. Recordings were only analysed if neuronal transients were clearly visible in the Miniscope recording and the imaged population of neurons was within CA1 of the hippocampus (Fig. 13b). Two recordings were analysed; one from an iTDP-43^{A315T} mouse and one from a control mouse.

Accepted Miniscope recordings were then passed through an analysis pipeline. This pipeline was developed as part the present study and implemented in a Python script within the Jupyter notebook environment, which called the CaImAn and miniscoPy libraries. The final script was

modified from the CaImAn/demo_pipeline_cnmfE.ipynb and miniscoPy/main_cnmfe_e.ipynb notebooks, available in their respective GitHub repositories (https://github.com/flatironinstitute/CaImAn; https://github.com/PeyracheLab/miniscoPy; Fig. 13c; Supp. 3). Movies were passed through the NoRMCorre, CNMF-E and OASIS libraries, to output a motion-corrected, denoised and deconvolved movie (Fig. 13d, e), and corresponding fluorescence traces (Fig. 13f).

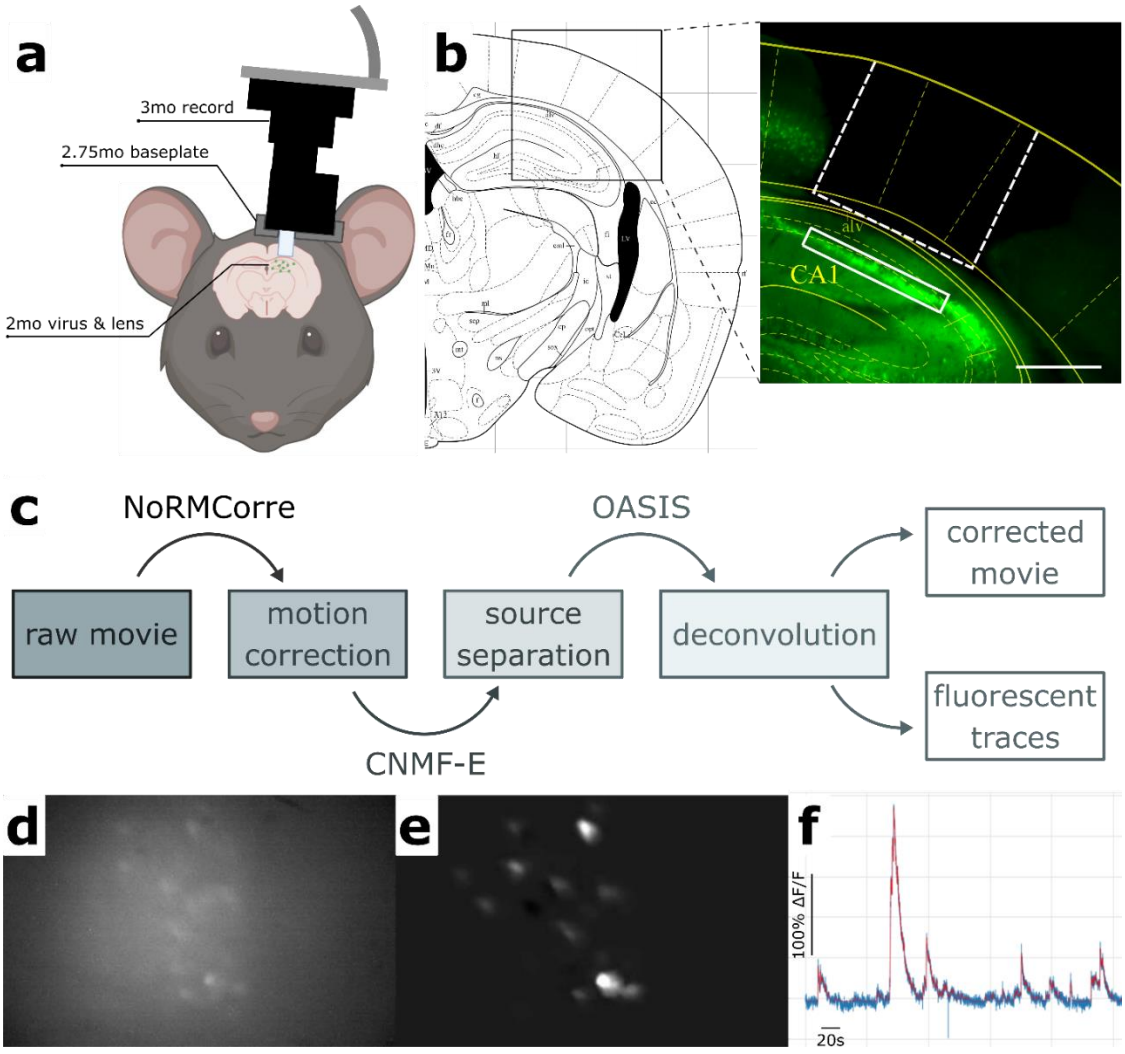

Figure 13: Miniscope protocol and analysis pipeline **a.** The Miniscope integrated fluorescent microscope was implanted into the hippocampus above CA1. **b.** Representative coronal section following imaging, showing lens implantation tract (*white dotted line*) and imaged neuronal population in CA1 (*white solid line*), with atlas overlay (*yellow line*). *Scale bar:* 500µm **c.** The data analysis pipeline, combining elements from the CaImAn and miniscoPy Python packages. **d.** Representative raw Miniscope input from iTDP-43^{A315T} control mouse with the **e.** corrected movie output and **f.** representative fluorescent trace.

3.6 Neuronal signalling in iTDP-43^{A315T} mice

3.6.1 Component analysis of Miniscope recordings

On successful implantation, anywhere from 20 to 200 neurons are typically visible in a Miniscope recording. This fluctuation may be due to target site differences but may also arise from variation between animals. After motion correction with NoRMCorre, comparable correlation images were generated from iTDP-43^{A315T} and control mice (Fig. 14a). After adjusting for the peak-to-noise ratio, 48 neurons in the control mouse and 25 neurons in the iTDP-43^{A315T} mouse were accepted for further analysis (Fig. 14b).

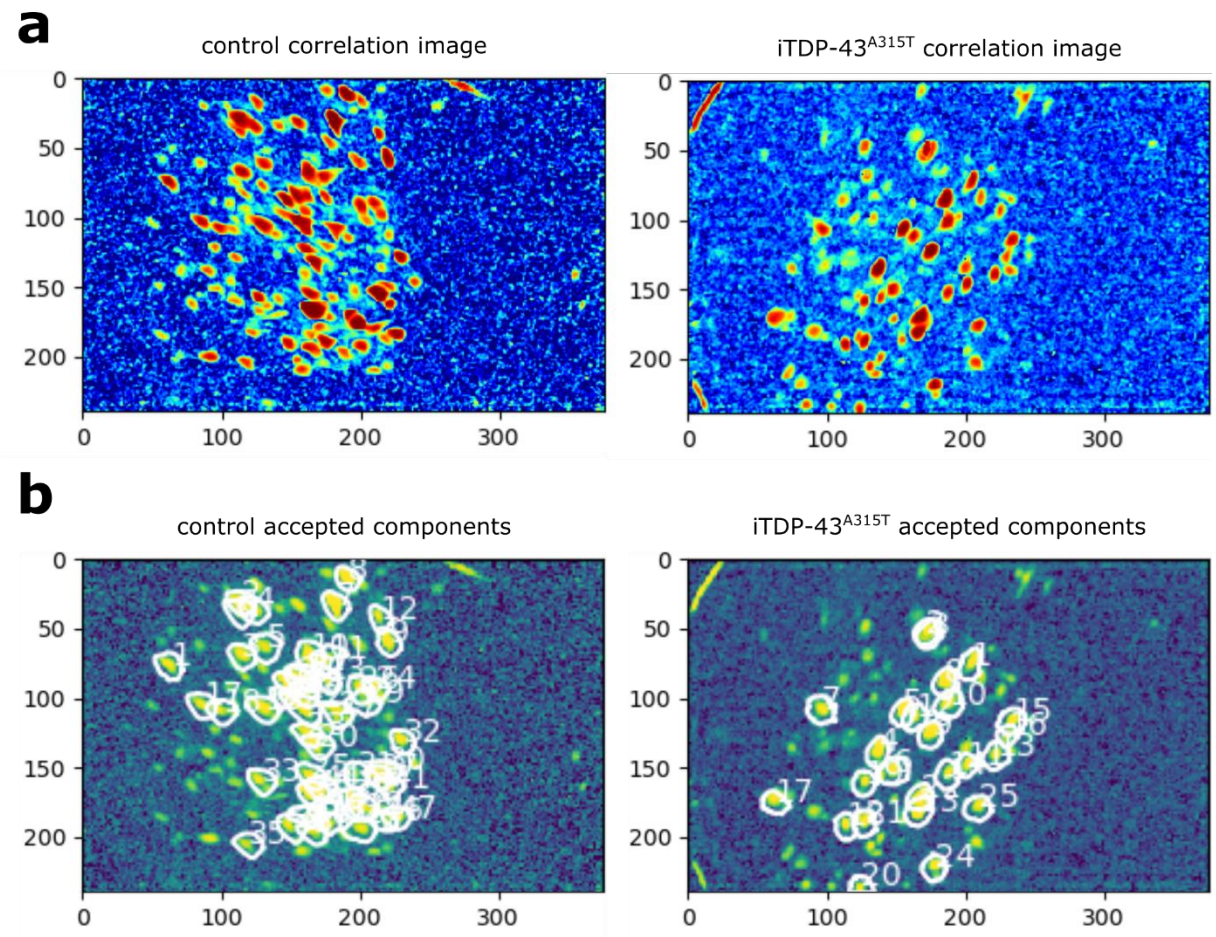

Figure 14: Components identified in iTDP-43^{A315T} and control mice. **a.** Correlation image, identifying synchronicity between neighbouring groups of pixels. **b.** Final component map. 48 components were accepted as neurons in the control mouse and 25 neurons in the transgenic iTDP-43^{A315T} mouse, based on pixel correlation and peak-noise ratio.

3.6.2 TDP-43^{A315T} alters neuronal signalling in mice

Output movies of selected neurons showed fewer visible calcium transients in iTDP-43^{A315T} mouse compared to control, despite comparable number of neurons analysed (Fig. 15a, b; *upper*). Further analysis of individual fluorescence traces revealed differences in individual neuronal activity levels (Fig. 15a, b; *lower*). In the control mouse, neurons were active 71.01±2.45% of the time, while neuronal activity was significantly lower at 34.66±4.17% of the time in iTDP-43^{A315T} transgenic mouse (Fig. 15c). Accordingly, 34.08±1.18 neurons had activity levels over baseline in the control mouse brain; while only 8.67±1.04 neurons were signalling over baseline in the transgenic mouse, in any given frame on average (Fig. 15d).

Moreover, the shape of calcium fluorescence traces was different in control and iTDP-43^{A315T} neurons. Neurons from the iTDP-43^{A315T} mouse showed compact calcium signals, while neurons from the control mouse produced a noisier trace. While there were roughly similar numbers of synchronous calcium events, event duration in control neurons was significantly longer than in iTDP-43^{A315T} neurons (8.73±0.41s in control, 6.54±0.86s in iTDP-43^{A315T}; Fig. 15e), paralleling results seen *in vitro*.

Taken together, we see that fewer neurons are present in the iTDP-43^{A315T} disease model, and the neurons that are present are less active. These decreased activity levels appear to be a result of reductions in event duration in transgenic mice, providing evidence for signalling and excitability changes in disease.

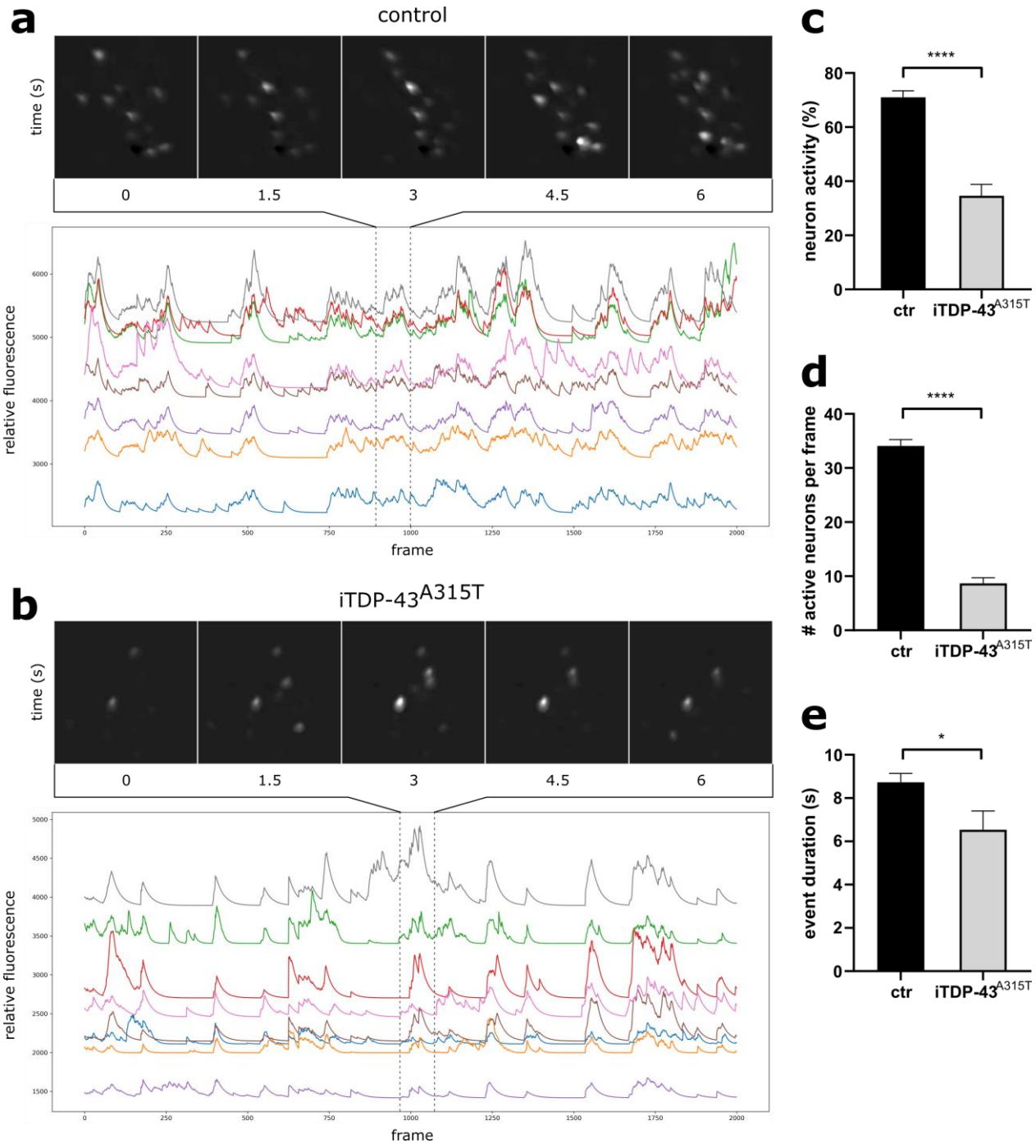

Figure 15: Miniscope recordings and traces from transgenic iTDP-43^{A315T} and control mice. **a.** A representative 6 second interval from the corrected Miniscope recordings (*upper*), with 8 representative fluorescent traces of neuronal activity over 2000 frames (*lower*), taken from a control mouse. **b.** Representative movie frames (*upper*) and fluorescent traces (*lower*) taken from an iTDP-43^{A315T} transgenic mouse as above. Fewer neurons were visible in the transgenic recording in any given frame, and calcium events were shorter in duration. **c.** Quantification of activity per neuron as a percentage of recording time shows reduced activity in iTDP-43^{A315T} transgenic neurons. **d**. Quantification of active neurons per frame shows fewer visible neurons in iTDP-43^{A315T} neurons compared to control. **e.** Reductions in neuron activity in iTDP-43^{A315T} mice were due to reductions in event duration. (*, $P < 0.05$; ****, $P < 0.0001$; n = 8 neurons per group).

4 Discussion

The current literature is unclear as to the nature of excitability changes in MND and FTD. Historically, studies have suggested that hyperexcitability leads to excitotoxicity and cell death in motor neurons, and clinical trials are largely focused on reducing neuronal excitability and oxidative stress (Vucic, Nicholson & Kiernan, 2008; Carbone et al., 2012; Rothstein, 2017). However, more recent studies suggest that neurons shift from a hyperexcitable to a hypoexcitable state as disease progresses, and it is the hypoexcitable population of neurons that are most vulnerable to neurodegeneration (Delestrée et al., 2014; Martinez-Silva et al., 2018). Still other studies suggest that disease progression is due to neither outright hyper- nor hypoexcitability, but rather more nuanced changes in neuromodulation (Devlin et al., 2015). Therefore, two model systems were established in the current study to better understand excitability changes in disease and elucidate disease mechanisms in MND and FTD.

This discussion is structured into three main sections, which together provide an assessment of the soundness and significance of these two models. Section 4.1 assesses the validity and limitations of each model, first in the primary neuron system, and then in the iTDP-43^{A315T} Miniscope system. Section 4.2 then synthesises the results obtained from these two models in the broader context of calcium signalling and excitability. Finally, Section 4.3 covers the research questions that are raised, and future directions for this work.

4.1 Establishing models of neuronal signalling in MND/FTD

In both models outlined here, the GCaMP family of calcium indicators was selected for functional readout of neuronal signalling patterns, using calcium signalling as a proxy for signalling activity (Tian et al., 2009). When using calcium indicators from the GCaMP family, it is essential to accurately titrate expression levels to avoid excessive calcium binding and neurotoxicity (Resendez et al., 2016). The recent jGCaMP7f calcium sensor used in this study expresses enhanced calcium sensitivity when compared with previous generations of GCaMP, and favourable calcium kinetics for live imaging, with both a fast rise and decay time (Dana et al., 2018).

4.1.1 Calcium signalling in primary neurons

This study firstly aimed to establish a model to determine the effects of TDP-43 on neuronal signalling *in vitro*. Primary hippocampal cultures are commonly used as a model for interrogating disease mechanisms and have been used by our lab and others to great success in screening mutations or evaluating drug candidates (Fath et al., 2008, Bigini et al., 2002). Furthermore, in a tau model of neurodegenerative disease, a similar study design using calcium indicators provided compelling evidence of signalling changes (Patel et al., 2015). In the present study, therefore, primary neurons were transduced with selected TDP-43 variants together with jGCaMP7f to characterise the effects of TDP-43 related variants on neuronal signalling. Complete transduction of AAV PHP.B TDP-43 variants and jGCaMP7f constructs was achieved as shown by immunocytochemistry, and western blot confirmed that protein expression levels of transduced constructs did not change greatly over time. Using live cell imaging, spontaneous calcium transients were visible from 12 DIV onwards and cells remained viable until at least 20 DIV, at which point they were PFA-fixed. Together, this demonstrates validity of the system, with appropriate expression of the target constructs and cell viability over the duration of recording.

However, there were two notable limitations of the co-transduction system implemented in primary cultures. Firstly, co-transduction as opposed to single transduction raises questions regarding transduction efficiency. This confounds the results seen in jGCaMP7f fluorescence, and causes difficulties distinguishing between true differences in calcium levels, and differences in jGCaMP7f reporter levels. This problem could be mitigated by co-transducing with a suitable empty vector control, such as CAG-mRuby2. Secondly, during live-cell recordings it is impossible to distinguish which cells have been successfully transduced with TDP-43 due. To a degree, viral transduction efficiencies may be inferred from ICC post experimentation, however, the entire field of view must be assumed to equally express each TDP-43 variant, as neurons move dynamically over the duration of the experiment. As such, while signalling differences observed between neurons on a coverslip may be due to variations in TDP-43 variant expression levels, expression changes between individual cells were not measured. This could be circumvented by instead using TDP-43-mRuby2 variant constructs, which would allow dynamic identification of transduced neurons. Unfortunately, there was insufficient time to complete this study due to unforeseen neuronal toxicity, however titration of the TDP-43-mRuby2 constructs remains as a future experiment.

4.1.2 iTDP-43^{A315T} Miniscope recordings

There are a number of recording techniques available for *in vivo* imaging in mouse models, each with different capabilities and spatiotemporal resolutions (Fig. 16). These can generally be classified as either electrophysiological techniques (electroencephalography, electrode arrays, and whole-cell patch-clamping; *yellow*) or optical techniques (microscopy; *green*; Aharoni & Hoogland, 2019). To accurately record calcium dynamics in intercellular interactions, it is necessary to record from relatively large regions at the single cell resolution. Furthermore, imaging in freely behaving animals allows for an accurate readout of brain signalling during normal function. Miniaturised integrated microscope systems, such as the Miniscope used in this project, sit at the intersection of these capabilities, and are uniquely positioned to provide novel disease insights.

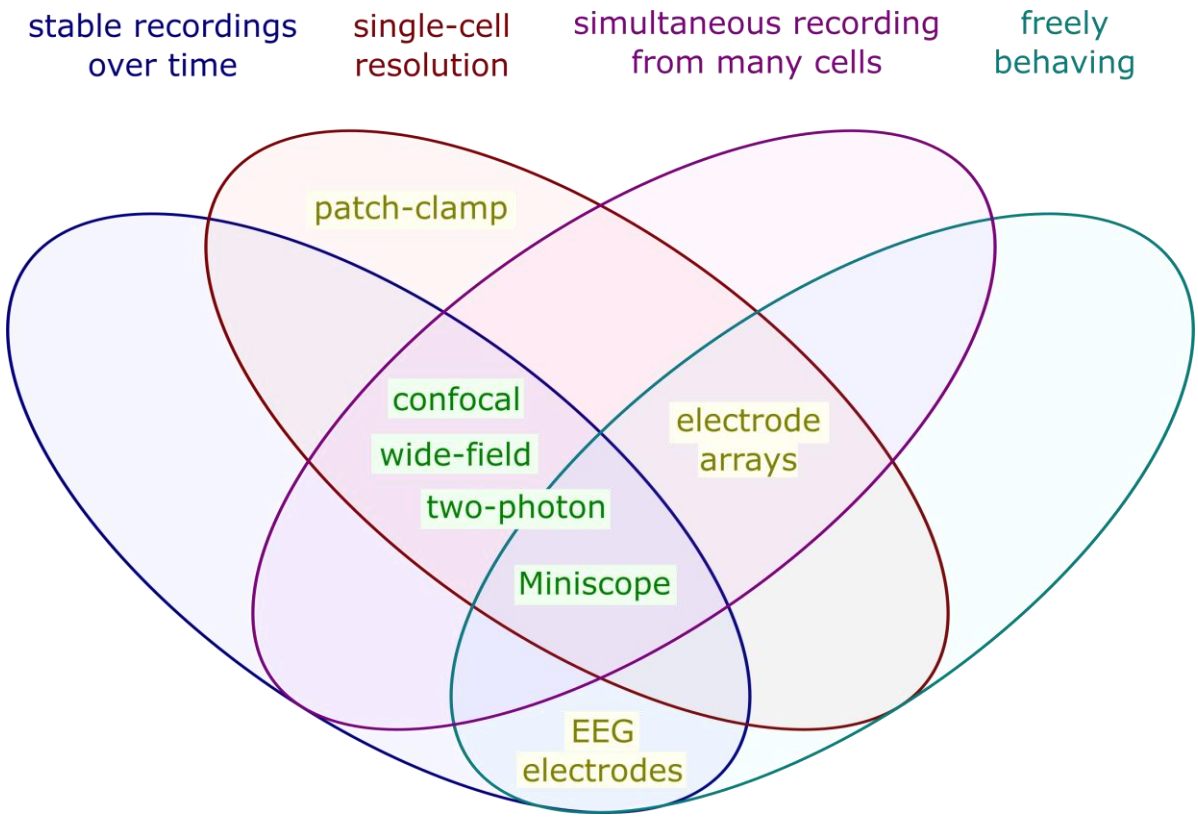

Figure 16: Overview of recording techniques available for in vivo imaging of mice. *Yellow:* Electrophysiological techniques. *Green:* microscopy techniques.

EEG = electroencephalography.

Integrated microscope systems, such as the Miniscope, have typically been used to investigate physiological functions of various brain regions and neuronal subpopulations. Only most recently has the integrated microscope system from Inscopix (Ghosh et al., 2011) been applied in disease, with a mouse model of narcolepsy (Sun, Bendell, & Liu, 2019), and to our

knowledge this is the first application of an integrated microscope in a neurodegenerative disease model. As a model of MND/FTD, iTDP-43^{A315T} mice experience brain atrophy and reduction in total brain volume, which initially posed a concern as to the accuracy of the Miniscope implantation procedure. However, linear transformation of the target coordinates for viral injection and lens implantation based on proportional distance between bregma and lambda gave excellent results with no further adjustments necessary, as confirmed by histological sectioning. Using these adjusted coordinates, recordings were obtained of similar quality to previously published results (Cai et al., 2016) in both iTDP-43^{A315T} and control mice, providing promising evidence of system suitability in disease models.

However, the Miniscope work showcased in this thesis is primarily presented as proof-of-concept, and there is still much work to be done. Most notably, this study only presents recordings and analysis from two animals, one each from the iTDP-43^{A315T} and control cohort. While a much larger cohort of animals were initially prepared for surgical procedures, many were excluded from later analysis due to off-target injection or implantation. The Miniscope implantation has very low tolerances (±50µm), as the target neuronal population must be accurately injected with jGCaMP7f virus, and the lens implant placed 2-300µm superior. Although these issues were anticipated prior to commencement of the study, with a higher number of mice enrolled initially, time constraints for this thesis limited further extension of the sample size (Supp. 6 contains a complete list of mouse surgery sites tested, with rationale and results). Accordingly, statistical analyses of neuronal activity were performed on eight representative neurons from each animal. Future work with this system will initially focus on further optimisation of the Miniscope surgical protocol to increase surgical success rate. Upon successful optimisation, sample size for animal work will then be increased to n=8, as is standard for this technique.

While the Miniscope system is a technological advancement in the field of neurodegenerative diseases, there are nevertheless limitations to the system. Firstly, not all neurons of iTDP-43^{A315T} mice express transgenic human TDP-43^{A315T} and live-cell recording of calcium activity will not be able to distinguish transgenic from non-transgenic cells in real time. This parallels the limitations observed in the primary hippocampal system. One way to overcome this is to establish a parallel system in wild type mice with expression of fluorescence-labelled TDP-43 variants via AAV transduction. In conjunction with a second excitation/emission filter set, this would enable in vivo identification of AAV-mediated TDP-43 expressing cells, adding further validity to these results.

The other major confounding factor to the current Miniscope system is the effects of locomotion on live recording as it is known to alter neuronal spiking activity. For instance, Purkinje neurons of the cerebellum are known to exhibit differential rates of calcium signalling during motor tasks, with the greatest activity during locomotion, and the least activity during rest (Ghosh et al., 2011). Additionally, there is a discrepancy in calcium excitation patterns in place cells of the hippocampal CA1 which respond to mouse location (Ziv et al., 2013). These problems may be circumvented by synchronous recording of animal behaviour with a video camera. Accordingly, Miniscope recordings can be scored and partitioned for analysis based on animal behaviour, overcoming the limitation to the interpretation of recordings due to movement of mice.

4.2 Excitability changes in MND/FTD

In combination, the in vitro primary culture model and the in vivo Miniscope model serve as a starting point for understanding excitability changes in disease. While there are limitations in both models, together they nevertheless provide intriguing preliminary evidence of signalling changes in MND/FTD. The results presented from these two models may be summarised into two primary observations. Firstly, in the presence TDP-43 variant expression, a decreased calcium response was detected during neuronal signalling. Secondly, TDP-43 expression was also observed to increase spiking synchronicity, thereby altering neuronal signalling dynamics.

4.2.1 TDP-43 expression reduces calcium response to signalling activity

In primary hippocampal neurons TDP-43 transduction was observed to decrease neuronal calcium response during spontaneous neuronal activation. Specifically, at later time points control neurons displayed much greater calcium response than earlier time points, while TDP-43 neurons showed similar levels of calcium fluorescence over the duration of imaging. Transduction of all TDP-43 variants decreased calcium response to spontaneous electrical stimulation, with wild-type TDP-43 and TDP-43 harbouring the A315T disease mutation functioning very similarly. The greatest reduction was seen in cells transduced with the functional TDP-43-ΔNLS mutant which failed to increase in calcium response over the duration of recording.

There may be two reasons that led to a decrease in calcium response across all TDP-43 variants. Firstly, TDP-43 downregulates its own expression by binding to its RNA transcript (Sephton et al., 2012). Expression of wild-type human TDP-43 has been shown to downregulate the production of endogenous TDP-43, disrupting its function and causing neurodegeneration (Igaz

et al., 2011). If transgenic human TDP-43 is unable to compensate for this loss, there may be a loss-of-function effect, explaining the dysfunctional calcium response observed in these neurons. Secondly, while all AAV PHP.B TDP-43 variant transduced neurons TDP-43 functioned as overexpression systems, TDP-43-ΔNLS transduced cells displayed the strongest cytoplasmic expression. Indeed, this functional change is the fundamental feature of TDP-43-ΔNLS (Winton et al., 2008). The decreased calcium response during spontaneous activity was present in all TDP-43 variants but was most pronounced in ΔNLS transduced cells. Since there are decreasing levels of calcium fluorescence with increasing cytoplasmic TDP-43, excessive cytoplasmic TDP-43 may also decrease calcium response to signalling. This result is of particular interest as cytoplasmic TDP-43 levels best correlate with disease severity across all disease models (Barmada et al., 2010).

The decreased calcium fluorescence observed in this model may be due to changes in electrophysiological measures of neuronal health, or dysfunctions in calcium buffering. Electrophysiological studies have reported a depolarisation in resting membrane potential in various neuronal models of disease (Devlin et al., 2015). Conversely, low cytoplasmic calcium buffering capacity, concomitant with a reduction in calcium binding proteins in disease is a well-established result in MND/FTD (Bernard-Marissal et al., 2012; Alexianu et al., 1994). Therefore, either mechanism presents a reasonable explanation for the reduced calcium response observed here. However, the present experimental design cannot distinguish between effects of calcium homeostasis and those of amplitude response. As such, future work with this model will establish a parallel measure of excitability to disentangle these two effects. For instance, an in vitro microelectrode array system would inform of specific changes in excitability in the presence of TDP-43.

However, there are several points for careful consideration before direct translation of calcium fluorescence into a readout of calcium response. Changes in calcium fluorescence in the present AAV-transduced primary culture system should represent changes in intracellular calcium levels. Yet, changes in fluorescence reflect not only calcium levels but are also a function of fluctuations in jGCaMP7f reporter levels. Therefore, this study accounted for jGCaMP7f levels by probing for GFP by western blot in neurons at 12 DIV and 20 DIV, corresponding to the start and end of recordings. While there was some variance in jGCaMP7f levels between groups, levels of jGCaMP7f did not increase between 12 and 20 DIV, while cell fluorescence increased greatly in the single transduced wells over time. Therefore, while the ideal control group would be co-transduced with an empty vector control, such as AAV-CAG-mRuby2

outlined above, these data nevertheless suggest that TDP-43 transduction decreases calcium response in cells, consistent with previous reports.

While it would be worthwhile to confirm replication of calcium response in vivo, absolute fluorescence data cannot be gathered from the Miniscope system, since there is significant variability in sample fluorescence dependent on light diffusion, imaging depth, background signal, and other factors (Resendez et al., 2016). As such, the Miniscope was calibrated to record at an LED value that gave the strongest signal to noise ratio, and the amplitude of signal traces is not directly comparable to results from primary hippocampal cultures.

4.2.2 TDP-43 expression alters signalling dynamics

Expression of TDP-43 also altered signalling patterns in both model systems. Calcium event duration increased over time in control primary cultures, while TDP-43 transduced neurons displayed no such increase. TDP-43 transduced cells showed significantly decreased event duration in calcium events when compared to control cells, with the shortest event duration observed in TDP-43-A315T transduced cells. This result was replicated in the Miniscope system, where calcium event duration was significantly reduced in an iTDP-43^{A315T} mouse model when compared to control. As such, neurons from the iTDP-43^{A315T} mouse were significantly less active, when compared to control. According to the acceptance criteria, there were fewer neurons recorded in the iTDP-43^{A315T} mouse recording. However, this reduction in accepted components likely reflects a difference in total underlying hippocampal neurons, given that iTDP-43^{A315T} mice have previously been reported to experience significant loss of hippocampal neurons (Ke et al., 2015).

In primary hippocampal cultures, the decrease in calcium event duration may have been due to a reduction in fluorescence in TDP-43 transduced neurons compared to control. In neuronal cultures with brighter fluoresce, calcium transients are visible for longer and these neurons thus appear to signal for longer. To mitigate this issue, event duration was operationalised as lasting from the initialisation of the first spike to the initialisation of the last spike in a spike train. Even so, TDP-43 transduced cells experienced decreased event duration, with the shortest events occurring in TDP-43-A315T neuronal cultures.

It is interesting to note that TDP-43-A315T transduced neurons were the most synchronous in calcium signalling response, as compared to TDP-43-WT and -ΔNLS neurons, with the least synchronicity observed in control neurons. On the other hand, TDP-43-ΔNLS showed the greatest reduction in calcium signalling compared to control, with no significant differences observed in levels between TDP-43-WT and -A315T. This difference indicates that these two

observations are related to different functions of TDP-43. TDP-43-ΔNLS is a functional mutant of TDP-43 lacking the NLS sequence required for localisation of TDP-43 to the nucleus. As such its cytoplasmic localisation may affect calcium buffering and homeostasis. On the other hand, TDP-43-A315T is a disease mutant of TDP-43 and so the phenotype observed in signalling duration is perhaps a better representation of the MND/FTD disease state. As changes in calcium buffering did not seem to cause reduced signalling duration (and vice versa), it seems that the roles of TDP-43 in intracellular calcium homeostasis and in spiking activity may be less related that initially hypothesised.

Notably, despite differences in calcium event duration, each stimulated neuron fired only once in any given signalling event across all cultures. As such, the longer event duration observed in control cultures was not due to repeat firing of hippocampal neurons. Rather, these cultures experienced slower stimulus propagation across the FOV. This was in line with previous descriptions of synaptic modification and strengthening in developmental neurons (Patel et al., 2015). In contrast, TDP-43-WT and -ΔNLS transduced cells fired with increased synchronicity, and TDP-43-A315T neurons fired almost instantaneously across the FOV.

One possible explanation for the increased synchronicity in TDP-43 systems is that TDP-43 mutant expression increases hyperexcitability and increases neuronal sensitivity to input. This would decrease input threshold for firing and result in more synchronous signalling, with less delay between signal transmission. TMS studies in MND patients report an increase in motor evoked potential (MEP) amplitude in response to a single stimulus. Furthermore, while control subjects normally experience short interval intracortical inhibition (SICI) in response to a subthreshold priming stimulus, MND patients have a greatly decreased SICI response (Vucic et al., 2013). These accounts indicate increased neuronal sensitivity to stimulation consistent with our data. If transduced neurons require less stimulation to fire, then even brief stimulation would be sufficient to induce depolarisation, increasing signalling simultaneity.

An alternate explanation is that decreased calcium event duration was a functional result of decreased signalling ability, due to neuronal hypoexcitability. Notably, a recent electrophysiological study showed initial response to electrical stimulation, but an inability to fire continuously on repeat stimulation in motor neurons from SOD1-G93A and FUS-P525L mice (Martinez-Silva et al., 2018). On inspection of the Miniscope fluorescence traces in the present study, the control mouse showed more peaks in each calcium event when compared to the iTDP-43^{A315T} transgenic mouse. In contrast, neurons from the iTDP-43^{A315T} mouse fired fewer times in each event before returning to baseline, suggesting decreased response to repeated stimulation. Overall, iTDP-43^{A315T} neurons were less active during the recording

duration, indicating that transgene expression led to hypoexcitability, confirming the results from Martinez-Silva et al. (2018).

The final explanation for these data is a combination of these two theories. Rather than outright hyper- or hypoexcitability, these observations instead may indicate multifaceted excitability changes. Neurons initially exhibit a stronger initial response to stimulus, suggesting a hyperexcitable state. This is evident from the hypersynchronicity observed in primary culture, indicating increased sensitivity. Furthermore, this result is consistent with the TMS data, which serve as one of the earliest diagnostic criteria evident in disease. However, neurons then fail to respond to repeat stimulation, as observed in the decreased spike train activity in iTDP-43^{A315T} mouse neurons. This confirms results seen in electrophysiological studies where decreased sensitivity to repeat stimulation occurs in the neuronal population most susceptible to disease (Martinez-Silva et al., 2018). Additionally, reports of patient-derived iPSCs indicate that there is a temporally defined profile of excitability changes in disease, with initial hyperexcitability followed by later hypoexcitability within a matter of weeks (Devlin et al., 2015). This temporal change may explain the differences between the two model systems described here, with hyperexcitability in the early neuronal model, and hypoexcitability in mature mouse neurons. Together, this paints a picture of ALS as a disease characterised by abnormal excitation patterns, with complex and multifaceted underlying mechanisms.

4.3 Future directions

Calcium imaging is an active area of research with many new techniques and applications in development, and future directions and applications of this work are multitudinous. Both model systems outlined here provide complementary platforms for investigating the disease state with distinctive advantages and unique applications.

Future work will initially focus on further optimisation of these systems, and development of appropriate controls. Firstly, further titration of the AAV PHP.B TDP-43-mRuby2 variant and empty vector constructs is required to determine a suitable MOI for use in primary hippocampal cultures. This will provide an appropriate empty vector control for co-transduction, as well as allowing for live tracking of cells successfully transduced with TDP-43 variants. Secondly, electrophysiological methods will be applied to the primary hippocampal system. Combination of calcium imaging and electrophysiological methods in primary neuronal cultures will allow for differentiation between dysfunctions in calcium homeostasis and changes in resting membrane potential or amplitude response. These developments will clarify the sequence of

events in disease and improve suitability of the primary culture model for mechanistic interrogation of disease processes.

The Miniscope system, with its unique spatiotemporal resolution, offers opportunities for novel insights into neuronal activity and, in this thesis, we capitalise on these strengths to present compelling preliminary data on signalling changes in disease. The first step required for future development of the Miniscope system is further optimisation of the surgical protocol, to improve success rate of Miniscope recordings. After this is completed, appropriate controls will then be developed. This work will include expansion of the Miniscope system for identification of fluorescently tagged proteins with a secondary filter set. Such a system would allow real-time identification of transduced neurons and differentiation from non-transduced neurons.

However, the true power of the Miniscope system is in its capacity to image not only at a single cell resolution, but also in freely behaving animals, and in stable long-term recordings (Aharoni & Hoogland, 2019). Therefore, this system could be expanded for use for simultaneous recording of calcium signalling during anxiety and memory tests, as iTDP-43^{A315T} mice are known to exhibit behavioural changes. In the present study mice were characterised at three months of age, which is the earliest time point possible using the Miniscope system. This can be further expanded in future studies looking at characterising signalling changes in mice longitudinally, modelling disease progression over time. These additions will provide deeper insights into neuronal signalling changes observed in MND/FTD.

4.4 Summary and conclusions

In this study, two complementary approaches are presented for the study of calcium signalling changes in TDP-43 models of disease. The former is an *in vitro* system using AAV to express TDP-43 variants together with a calcium sensor in mouse primary neuronal cultures. The latter uses an open source miniaturised microscope system to study real time calcium signalling in live iTDP-43^{A315T} transgenic and control mice with AAV-mediated calcium sensor. This Miniscope application in a neurodegenerative disease mouse model is the first of its kind in this field, with a huge potential in furthering our current understanding of neuronal signalling in live disease model. Results from both systems showed for the first time that mutant TDP-43 expression reduced the magnitude of spontaneous calcium signalling response but enhanced signalling synchronicity, likely due to excitability changes in disease state. Therefore, these models suggest a nuanced view should be taken when considering the relationship between excitability, neurodegeneration and disease. While this work is very much in its infancy, these initial results hold great promise for future developments in MND and FTD.

References

AFTDA. (2017). About FTD – the Australian Frontotemporal Dementia Association. Retrieved from https://theaftd.org.au/ on 16-06-2017.

Aharoni, D. B., & Hoogland, T. (2019). Circuit investigations with open-source miniaturized microscopes: past, present and future. *Frontiers in cellular neuroscience, 13*, 141.

Alexianu, M. E., Ho, B. K., Mohamed, A. H., La Bella, V., Smith, R. G., & Appel, S. H. (1994). The role of calcium-binding proteins in selective motoneuron vulnerability in amyotrophic lateral sclerosis. *Annals of Neurology: Official Journal of the American Neurological Association and the Child Neurology Society, 36*(6), 846-858.

Babin, P. J., Goizet, C., & Raldua, D. (2014). Zebrafish models of human motor neuron diseases: advantages and limitations. *Progress in neurobiology, 118*, 36-58.

Bagur, R., & Hajnóczky, G. (2017). Intracellular Ca2+ sensing: its role in calcium homeostasis and signaling. *Molecular cell, 66*(6), 780-788.

Barmada, S. J., Skibinski, G., Korb, E., Rao, E. J., Wu, J. Y., & Finkbeiner, S. (2010). Cytoplasmic mislocalization of TDP-43 is toxic to neurons and enhanced by a mutation associated with familial amyotrophic lateral sclerosis. *Journal of Neuroscience, 30*(2), 639-649.

Battaglioli, G., Martin, D. L., Plummer, J., & Messer, A. (1993). Synaptosomal glutamate uptake declines progressively in the spinal cord of a mutant mouse with motor neuron disease. *Journal of neurochemistry, 60*(4), 1567-1569.

Benavides, J., Camelin, J. C., Mitrani, N., Flamand, F., Uzan, A., Legrand, J. J., ... & Le Fur, G. (1985). 2-Amino-6-trifluoromethoxy benzothiazole, a possible antagonist of excitatory amino acid neurotransmission—II: Biochemical properties. *Neuropharmacology*, *24*(11), 1085-1092.

Bernard-Marissal, N., Moumen, A., Sunyach, C., Pellegrino, C., Dudley, K., Henderson, C. E., ... & Pettmann, B. (2012). Reduced calreticulin levels link endoplasmic reticulum stress and Fas-triggered cell death in motoneurons vulnerable to ALS. *Journal of Neuroscience, 32*(14), 4901-4912.

Bigini, P., Larini, S., Pasquali, C., Muzio, V., & Mennini, T. (2002). Acetyl-L-carnitine shows neuroprotective and neurotrophic activity in primary culture of rat embryo motoneurons. *Neuroscience letters, 329*(3), 334-338.

Blanco-Suarez, E., Liu, T. F., Kopelevich, A., & Allen, N. J. (2018). Astrocyte-secreted chordin-like 1 drives synapse maturation and limits plasticity by increasing synaptic GluA2 AMPA receptors. *Neuron, 100*(5), 1116-1132.

Bories, C., Amendola, J., Lamotte d'Incamps, B., & Durand, J. (2007). Early electrophysiological abnormalities in lumbar motoneurons in a transgenic mouse model of amyotrophic lateral sclerosis. *European Journal of Neuroscience, 25*(2), 451-459.

Brettschneider, J., Del Tredici, K., Irwin, D. J., Grossman, M., Robinson, J. L., Toledo, J. B., ... & Trojanowski, J. Q. (2014). Sequential distribution of pTDP-43 pathology in behavioral variant frontotemporal dementia (bvFTD). *Acta neuropathologica, 127*(3), 423-439.

Brettschneider, J., Del Tredici, K., Toledo, J. B., Robinson, J. L., Irwin, D. J., Grossman, M., ... & Trojanowski, J. Q. (2013). Stages of pTDP-43 pathology in amyotrophic lateral sclerosis. *Annals of neurology, 74*(1), 20-38.

Burrell, J. R., Halliday, G. M., Kril, J. J., Ittner, L. M., Götz, J., Kiernan, M. C., & Hodges, J. R. (2016). The frontotemporal dementia-motor neuron disease continuum. *The Lancet, 388*(10047), 919-931.

Cai, D. J., Aharoni, D., Shuman, T., Shobe, J., Biane, J., Song, W., ... & Silva, A. J. (2016). A shared neural ensemble links distinct contextual memories encoded close in time. *Nature, 534*(7605), 115.

Cannon, A., Yang, B., Knight, J., Farnham, I. M., Zhang, Y., Wuertzer, C. A., ... & Lewis, J. (2012). Neuronal sensitivity to TDP-43 overexpression is dependent on timing of induction. *Acta neuropathologica, 123*(6), 807-823.

Carbone, M., Duty, S., & Rattray, M. (2012). Riluzole elevates GLT-1 activity and levels in striatal astrocytes. *Neurochemistry international, 60*(1), 31-38.

Casci, I., & Pandey, U. B. (2015). A fruitful endeavor: modeling ALS in the fruit fly. *Brain research, 1607*, 47-74.

Chiang, P. M., Ling, J., Jeong, Y. H., Price, D. L., Aja, S. M., & Wong, P. C. (2010). Deletion of TDP-43 down-regulates Tbc1d1, a gene linked to obesity, and alters body fat metabolism. *Proceedings of the National Academy of Sciences, 107*(37), 16320-16324.

Choi, S. Y., Lopez-Gonzalez, R., Krishnan, G., Phillips, H. L., Li, A. N., Seeley, W. W., ... & Gao, F. B. (2019). C9ORF72-ALS/FTD-associated poly (GR) binds Atp5a1 and compromises mitochondrial function in vivo. *Nature neuroscience, 22*(6), 851.

Dana, H., Sun, Y., Mohar, B., Hulse, B., Hasseman, J. P., Tsegaye, G., ... & Kim, D. S. (2018). High-performance GFP-based calcium indicators for imaging activity in neuronal populations and microcompartments. *BioRxiv*, 434589.

de Carvalho, M., & Swash, M. (2013). Origin of fasciculations in amyotrophic lateral sclerosis and benign fasciculation syndrome. *JAMA neurology, 70*(12), 1562-1565.

DeJesus-Hernandez, M., Mackenzie, I. R., Boeve, B. F., Boxer, A. L., Baker, M., Rutherford, N. J., ... & Rademakers, R. (2011). Expanded GGGGCC hexanucleotide repeat in noncoding region of C9ORF72 causes chromosome 9p-linked FTD and ALS. *Neuron, 72*(2), 245-256.

Delestrée, N., Manuel, M., Iglesias, C., Elbasiouny, S. M., Heckman, C. J., & Zytnicki, D. (2014). Adult spinal motoneurones are not hyperexcitable in a mouse model of inherited amyotrophic lateral sclerosis. *The Journal of physiology, 592*(7), 1687-1703.

Deloitte (2015). Economic analysis of motor neurone disease in Australia. Accessed: 16-06-2017.

Devlin, A. C., Burr, K., Borooah, S., Foster, J. D., Cleary, E. M., Geti, I., ... & Miles, G. B. (2015). Human iPSC-derived motoneurons harbouring TARDBP or C9ORF72 ALS mutations are dysfunctional despite maintaining viability. *Nature communications, 6*, 5999.

Di Giorgio, F. P., Boulting, G. L., Bobrowicz, S., & Eggan, K. C. (2008). Human embryonic stem cell-derived motor neurons are sensitive to the toxic effect of glial cells carrying an ALS-causing mutation. *Cell stem cell, 3*(6), 637-648.

Durham, H. D., Roy, J., Dong, L., & Figlewicz, D. A. (1997). Aggregation of mutant Cu/Zn superoxide dismutase proteins in a culture model of ALS. *Journal of Neuropathology & Experimental Neurology, 56*(5), 523-530.

Fath, T., Ke, Y. D., Gunning, P., Götz, J., & Ittner, L. M. (2008). Primary support cultures of hippocampal and substantia nigra neurons. *Nature protocols, 4*(1), 78.

Fray, A. E., Ince, P. G., Banner, S. J., Milton, I. D., Usher, P. A., Cookson, M. R., & Shaw, P. J. (2003). The expression of the glial glutamate transporter protein EAAT2 in motor neuron disease: an immunohistochemical study. *European journal of neuroscience, 10*(8), 2481-2489.

Forrest, S. L., Halliday, G. M., McCann, H., McGeachie, A. B., McGinley, C. V., Hodges, J. R., ... & Kril, J. J. (2019). Heritability in frontotemporal tauopathies. *Alzheimer's & Dementia: Diagnosis, Assessment & Disease Monitoring, 11*, 115-124.

Fratta, P., Sivakumar, P., Humphrey, J., Lo, K., Ricketts, T., Oliveira, H., ... & Acevedo-Arozena A. (2018). Mice with endogenous TDP-43 mutations exhibit gain of splicing function and characteristics of amyotrophic lateral sclerosis. *The EMBO journal, 37*(11).

Gal, J., Zhang, J., Kwinter, D. M., Zhai, J., Jia, H., Jia, J., & Zhu, H. (2011). Nuclear localization sequence of FUS and induction of stress granules by ALS mutants. *Neurobiology of aging, 32*(12), 2323-e27.

Geevasinga, N., Menon, P., Nicholson, G. A., Ng, K., Howells, J., Kril, J. J., ... & Vucic, S. (2015). Cortical function in asymptomatic carriers and patients with C9orf72 amyotrophic lateral sclerosis. *JAMA neurology, 72*(11), 1268-1274.

Ghosh, K. K., Burns, L. D., Cocker, E. D., Nimmerjahn, A., Ziv, Y., El Gamal, A., & Schnitzer, M. J. (2011). Miniaturized integration of a fluorescence microscope. *Nature methods, 8*(10), 871.

Giovannucci, A., Friedrich, J., Gunn, P., Kalfon, J., Brown, B. L., Koay, S. A., ... & Pnevmatikakis, E. A. (2019). CaImAn an open source tool for scalable calcium imaging data analysis. *Elife, 8*, e38173.

Gordon, J., Amini, S., & White, M. K. (2013). General overview of neuronal cell culture. In *Neuronal Cell Culture* (pp. 1-8). Humana Press, Totowa, NJ.

Griffiths, E. J., & Rutter, G. A. (2009). Mitochondrial calcium as a key regulator of mitochondrial ATP production in mammalian cells. *Biochimica et Biophysica Acta (BBA)-Bioenergetics, 1787*(11), 1324-1333.

Hetz, C., & Saxena, S. (2017). ER stress and the unfolded protein response in neurodegeneration. *Nature Reviews Neurology, 13*(8), 477.

Igaz, L. M., Kwong, L. K., Lee, E. B., Chen-Plotkin, A., Swanson, E., Unger, T., ... & Lee, V. M. Y. (2011). Dysregulation of the ALS-associated gene TDP-43 leads to neuronal death and degeneration in mice. *The Journal of clinical investigation, 121*(2), 726-738.

Janssens, J., Wils, H., Kleinberger, G., Joris, G., Cuijt, I., Ceuterick-de Groote, C., ... & Kumar-Singh, S. (2013). Overexpression of ALS-associated p. M337V human TDP-43 in mice worsens disease features compared to wild-type human TDP-43 mice. *Molecular neurobiology, 48*(1), 22-35.

Jimenez, J. C., Su, K., Goldberg, A. R., Luna, V. M., Biane, J. S., Ordek, G., ... & Kheirbek, M. A. (2018). Anxiety cells in a hippocampal-hypothalamic circuit. *Neuron, 97*(3), 670-683.

Kanai, K., Kuwabara, S., Misawa, S., Tamura, N., Ogawara, K., Nakata, M., ... & Bostock, H. (2006). Altered axonal excitability properties in amyotrophic lateral sclerosis: impaired potassium channel function related to disease stage. *Brain, 129*(4), 953-962.

Ke, Y. D., van Hummel, A., Stevens, C. H., Gladbach, A., Ippati, S., Bi, M., ... & Ittner, L. M. (2015). Short-term suppression of A315T mutant human TDP-43 expression improves functional deficits in a novel inducible transgenic mouse model of FTLD-TDP and ALS. *Acta neuropathologica, 130*(5), 661-678.

Lagier-Tourenne, C., & Cleveland, D. W. (2009). Rethinking ALS: The FUS about TDP-43. *Cell, 136*(6), 1001-1004.

Lin, C. L. G., Bristol, L. A., Jin, L., Dykes-Hoberg, M., Crawford, T., Clawson, L., & Rothstein, J. D. (1998). Aberrant RNA processing in a neurodegenerative disease: the cause for absent EAAT2, a glutamate transporter, in amyotrophic lateral sclerosis. *Neuron, 20*(3), 589-602.

Ling, S. C., Polymenidou, M., & Cleveland, D. W. (2013). Converging mechanisms in ALS and FTD: disrupted RNA and protein homeostasis. *Neuron, 79*(3), 416-438.

Lee, S., & Huang, E. J. (2017). Modeling ALS and FTD with iPSC-derived neurons. *Brain research, 1656*, 88-97.

Martinez-Silva, M., Imhoff-Manuel, R. D., Sharma, A., Heckman, C. J., Shneider, N. A., Roselli, F., ... & Manuel, M. (2018). Hypoexcitability precedes denervation in the large fast-contracting motor units in two unrelated mouse models of ALS. *Elife, 7*, e30955.

Menon, P., Geevasinga, N., Yiannikas, C., Howells, J., Kiernan, M. C., & Vucic, S. (2015). Sensitivity and specificity of threshold tracking transcranial magnetic stimulation for diagnosis of amyotrophic lateral sclerosis: a prospective study. *The Lancet Neurology*, *14*(5), 478-484.

Neumann, M., Sampathu, D. M., Kwong, L. K., Truax, A. C., Micsenyi, M. C., Chou, T. T., ... & Lee, V. M. Y. (2006). Ubiquitinated TDP-43 in frontotemporal lobar degeneration and amyotrophic lateral sclerosis. *Science*, *314*(5796), 130-133.

NIH, U.S. National Library of Medicine. (2019). clinicaltrials.gov. Retrieved from https://clinicaltrials.gov on 27-06-2019.

Oakes, S. A., & Papa, F. R. (2015). The role of endoplasmic reticulum stress in human pathology. *Annual Review of Pathology: Mechanisms of Disease*, *10*, 173-194.

Palecek, J., Lips, M. B., & Keller, B. U. (1999). Calcium dynamics and buffering in motoneurones of the mouse spinal cord. *The Journal of physiology*, *520*(2), 485-502.

Patel, T. P., Man, K., Firestein, B. L., & Meaney, D. F. (2015). Automated quantification of neuronal networks and single-cell calcium dynamics using calcium imaging. *Journal of neuroscience methods*, *243*, 26-38.

Picher-Martel, V., Valdmanis, P. N., Gould, P. V., Julien, J. P., & Dupré, N. (2016). From animal models to human disease: a genetic approach for personalized medicine in ALS. *Acta neuropathologica communications*, *4*(1), 70.

Pnevmatikakis, E. A., & Giovannucci, A. (2017). NoRMCorre: An online algorithm for piecewise rigid motion correction of calcium imaging data. *Journal of neuroscience methods*, *291*, 83-94.

Pnevmatikakis, E. A., Soudry, D., Gao, Y., Machado, T. A., Merel, J., Pfau, D., ... & Paninski, L. (2016). Simultaneous denoising, deconvolution, and demixing of calcium imaging data. *Neuron*, *89*(2), 285-299.

Renton, A. E., Majounie, E., Waite, A., Simón-Sánchez, J., Rollinson, S., Gibbs, J. R., ... & Traynor, B. J. (2011). A hexanucleotide repeat expansion in C9ORF72 is the cause of chromosome 9p21-linked ALS-FTD. *Neuron*, *72*(2), 257-268.

Resendez, S. L., Jennings, J. H., Ung, R. L., Namboodiri, V. M. K., Zhou, Z. C., Otis, J. M., ... & Stuber, G. D. (2016). Visualization of cortical, subcortical and deep brain neural circuit dynamics during naturalistic mammalian behavior with head-mounted microscopes and chronically implanted lenses. *Nature protocols*, *11*(3), 566.

Ringholz, G., Appel, S. H., Bradshaw, M., Cooke, N., Mosnik, D., and Schulz, P. (2005). Prevalence and patterns of cognitive impairment in sporadic ALS. *Neurology*, *65*(4):586–590.

Rojas, F., Gonzalez, D., Cortes, N., Ampuero, E., Hernández, D. E., Fritz, E., ... & Van Zundert, B. (2015). Reactive oxygen species trigger motoneuron death in non-cell-autonomous models of ALS through activation of c-Abl signaling. *Frontiers in cellular neuroscience*, *9*, 203.

Rothstein, J. D. (2017). Edaravone: a new drug approved for ALS. *Cell, 171*(4), 725.

Rothstein, J. D., Martin, L. J., & Kuncl, R. W. (1992). Decreased glutamate transport by the brain and spinal cord in amyotrophic lateral sclerosis. *New England Journal of Medicine, 326*(22), 1464-1468.

Sareen, D., O'Rourke, J. G., Meera, P., Muhammad, A. K. M. G., Grant, S., Simpkinson, M., ... & Baloh, R. H. (2013). Targeting RNA foci in iPSC-derived motor neurons from ALS patients with a C9ORF72 repeat expansion. *Science translational medicine, 5*(208), 208ra149-208ra149.

Sasaki, S. (2010). Endoplasmic reticulum stress in motor neurons of the spinal cord in sporadic amyotrophic lateral sclerosis. *Journal of Neuropathology & Experimental Neurology, 69*(4), 346-355.

Schindelin, J., Arganda-Carreras, I., Frise, E., Kaynig, V., Longair, M., Pietzsch, T., ... & Cardona, A. (2012). Fiji: an open-source platform for biological-image analysis. *Nature methods, 9*(7), 676.

Sephton, C. F., Good, S. K., Atkin, S., Dewey, C. M., Mayer, P., Herz, J., & Yu, G. (2010). TDP-43 is a developmentally regulated protein essential for early embryonic development. *Journal of Biological Chemistry, 285*(9), 6826-6834.

Sephton, C. F., Cenik, B., Cenik, B. K., Herz, J., and Yu, G. (2012). TDP-43 in central nervous system development and function: clues to TDP-43-associated neurodegeneration. *Biological Chemistry, 393*(7):589-594.

Shaw, P. J., Forrest, V., Ince, P. G., Richardson, J. P., & Wastell, H. J. (1995). CSF and plasma amino acid levels in motor neuron disease: elevation of CSF glutamate in a subset of patients. *Neurodegeneration, 4*(2), 209-216.

Shi, Y., Lin, S., Staats, K. A., Li, Y., Chang, W. H., Hung, S. T., ... & Ichida, J. K. (2018). Haploinsufficiency leads to neurodegeneration in C9ORF72 ALS/FTD human induced motor neurons. *Nature medicine, 24*(3), 313.

Stallings, N. R., Puttaparthi, K., Luther, C. M., Burns, D. K., & Elliott, J. L. (2010). Progressive motor weakness in transgenic mice expressing human TDP-43. *Neurobiology of disease, 40*(2), 404-414.

Stoica, R., Paillusson, S., Gomez-Suaga, P., Mitchell, J. C., Lau, D. H., Gray, E. H., ... & Miller, C. C. (2016). ALS/FTD-associated FUS activates GSK-3β to disrupt the VAPB–PTPIP51 interaction and ER–mitochondria associations. *EMBO reports, 17*(9), 1326-1342.

Sun, Y., Bendell, E., & Liu, M. (2019). Activity dynamics of amygdala GABAergic neurons during cataplexy of narcolepsy. *eLife, 8*.

Swarup, V., Phaneuf, D., Bareil, C., Robertson, J., Rouleau, G. A., Kriz, J., & Julien, J. P. (2011). Pathological hallmarks of amyotrophic lateral sclerosis/frontotemporal lobar

degeneration in transgenic mice produced with TDP-43 genomic fragments. *Brain, 134*(9), 2610-2626.

Tadic, V., Prell, T., Lautenschlaeger, J., & Grosskreutz, J. (2014). The ER mitochondria calcium cycle and ER stress response as therapeutic targets in amyotrophic lateral sclerosis. *Frontiers in cellular neuroscience, 8,* 147.

Tan, R. H., Ke, Y. D., Ittner, L. M., & Halliday, G. M. (2017). ALS/FTLD: experimental models and reality. *Acta neuropathologica, 133*(2), 177-196.

Therrien, M., & Parker, J. A. (2014). Worming forward: amyotrophic lateral sclerosis toxicity mechanisms and genetic interactions in Caenorhabditis elegans. *Frontiers in genetics, 5,* 85.

Tian, L., Hires, S. A., Mao, T., Huber, D., Chiappe, M. E., Chalasani, S. H., ... & Looger, L. L. (2009). Imaging neural activity in worms, flies and mice with improved GCaMP calcium indicators. *Nature methods, 6*(12), 875.

Tollervey, J. R., Curk, T., Rogelj, B., Briese, M., Cereda, M., Kayikci, M., ... & Ule, J. (2011). Characterizing the RNA targets and position-dependent splicing regulation by TDP-43. *Nature neuroscience, 14*(4), 452.

Van Damme, P., Braeken, D., Callewaert, G., Robberecht, W., & Van Den Bosch, L. (2005). GluR2 deficiency accelerates motor neuron degeneration in a mouse model of amyotrophic lateral sclerosis. *Journal of Neuropathology & Experimental Neurology, 64*(7), 605-612.

van Hummel, A., Chan, G., van der Hoven, J., Morsch, M., Ippati, S., Suh, L., ... & Ke Y. D. (2018). Selective Spatiotemporal Vulnerability of Central Nervous System Neurons to Pathologic TAR DNA-Binding Protein 43 in Aged Transgenic Mice. *The American journal of pathology, 188*(6), 1447-1456.

Van Zundert, B., Peuscher, M. H., Hynynen, M., Chen, A., Neve, R. L., Brown, R. H., ... & Bellingham, M. C. (2008). Neonatal neuronal circuitry shows hyperexcitable disturbance in a mouse model of the adult-onset neurodegenerative disease amyotrophic lateral sclerosis. *Journal of Neuroscience, 28*(43), 10864-10874.

Verstraete, E., Van Den Heuvel, M. P., Veldink, J. H., Blanken, N., Mandl, R. C., Pol, H. E. H., & van den Berg, L. H. (2010). Motor network degeneration in amyotrophic lateral sclerosis: a structural and functional connectivity study. *PloS one, 5*(10), e13664.

Vucic, S., Nicholson, G. A., & Kiernan, M. C. (2008). Cortical hyperexcitability may precede the onset of familial amyotrophic lateral sclerosis. *Brain, 131*(6), 1540-1550.

Vucic, S., Ziemann, U., Eisen, A., Hallett, M., & Kiernan, M. C. (2013). Transcranial magnetic stimulation and amyotrophic lateral sclerosis: pathophysiological insights. *J Neurol Neurosurg Psychiatry, 84*(10), 1161-1170.

Wainger, B. J., Kiskinis, E., Mellin, C., Wiskow, O., Han, S. S., Sandoe, J., ... & Woolf, C. J. (2014). Intrinsic membrane hyperexcitability of amyotrophic lateral sclerosis patient-derived motor neurons. *Cell reports, 7*(1), 1-11.

Walker, A. K., Spiller, K. J., Ge, G., Zheng, A., Xu, Y., Zhou, M., ... & Lee, V. M. Y. (2015). Functional recovery in new mouse models of ALS/FTLD after clearance of pathological cytoplasmic TDP-43. *Acta neuropathologica, 130*(5), 643-660.

Wils, H., Kleinberger, G., Janssens, J., Pereson, S., Joris, G., Cuijt, I., ... & Kumar-Singh, S. (2010). TDP-43 transgenic mice develop spastic paralysis and neuronal inclusions characteristic of ALS and frontotemporal lobar degeneration. *Proceedings of the National Academy of Sciences, 107*(8), 3858-3863.

Winton, M. J., Igaz, L. M., Wong, M. M., Kwong, L. K., Trojanowski, J. Q., & Lee, V. M. Y. (2008). Disturbance of nuclear and cytoplasmic TAR DNA-binding protein (TDP-43) induces disease-like redistribution, sequestration, and aggregate formation. *Journal of Biological Chemistry, 283*(19), 13302-13309.

White, M. A., Kim, E., Duffy, A., Adalbert, R., Phillips, B. U., Peters, O. M., ... & Sreedharan, J. (2018). TDP-43 gains function due to perturbed autoregulation in a Tardbp knock-in mouse model of ALS-FTD. *Nature neuroscience, 21*(4), 552.

Wu, L. S., Cheng, W. C., Hou, S. C., Yan, Y. T., Jiang, S. T., & Shen, C. K. J. (2010). TDP-43, a neuro-pathosignature factor, is essential for early mouse embryogenesis. *Genesis, 48*(1), 56-62.

Xu, Y. F., Gendron, T. F., Zhang, Y. J., Lin, W. L., D'Alton, S., Sheng, H., ... & Petrucelli, L. (2010). Wild-type human TDP-43 expression causes TDP-43 phosphorylation, mitochondrial aggregation, motor deficits, and early mortality in transgenic mice. *Journal of Neuroscience, 30*(32), 10851-10859.

Yang, Y. M., Gupta, S. K., Kim, K. J., Powers, B. E., Cerqueira, A., Wainger, B. J., ... & Rubin, L. L. (2013). A small molecule screen in stem-cell-derived motor neurons identifies a kinase inhibitor as a candidate therapeutic for ALS. *Cell stem cell, 12*(6), 713-726.

Zhong, Z., Deane, R., Ali, Z., Parisi, M., Shapovalov, Y., O'Banion, M. K., ... & Zlokovic, B. V. (2008). ALS-causing SOD1 mutants generate vascular changes prior to motor neuron degeneration. *Nature neuroscience, 11*(4), 420.

Ziv, Y., Burns, L. D., Cocker, E. D., Hamel, E. O., Ghosh, K. K., Kitch, L. J., ... & Schnitzer, M. J. (2013). Long-term dynamics of CA1 hippocampal place codes. *Nature neuroscience, 16*(3), 264.

Supplementary Data

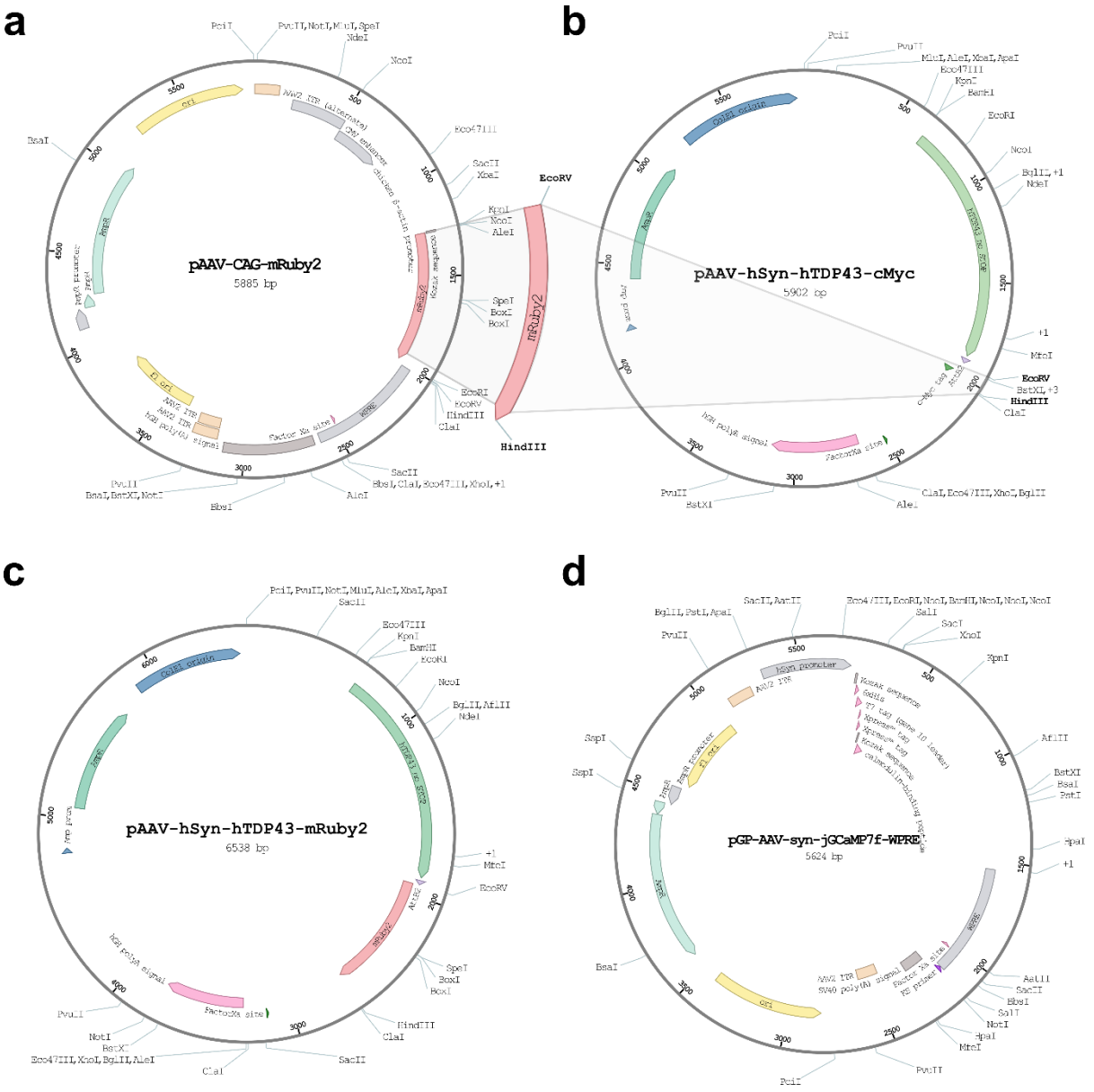

Supplementary 1: Plasmid maps for **a.** pAAV-CAG-mRuby2 (99123), showing mRuby2 fragment excised with *Eco*RV and *Hind*III sites added by PCR **b.** pAAV-hSyn-TDP-43-myc, showing insert site for mRuby2 fragment to generate **c.** pAAV-hSyn-TDP-43-mRuby2 **d.** pGP-AAV-syn-jGCaMP7f-WPRE (104488).

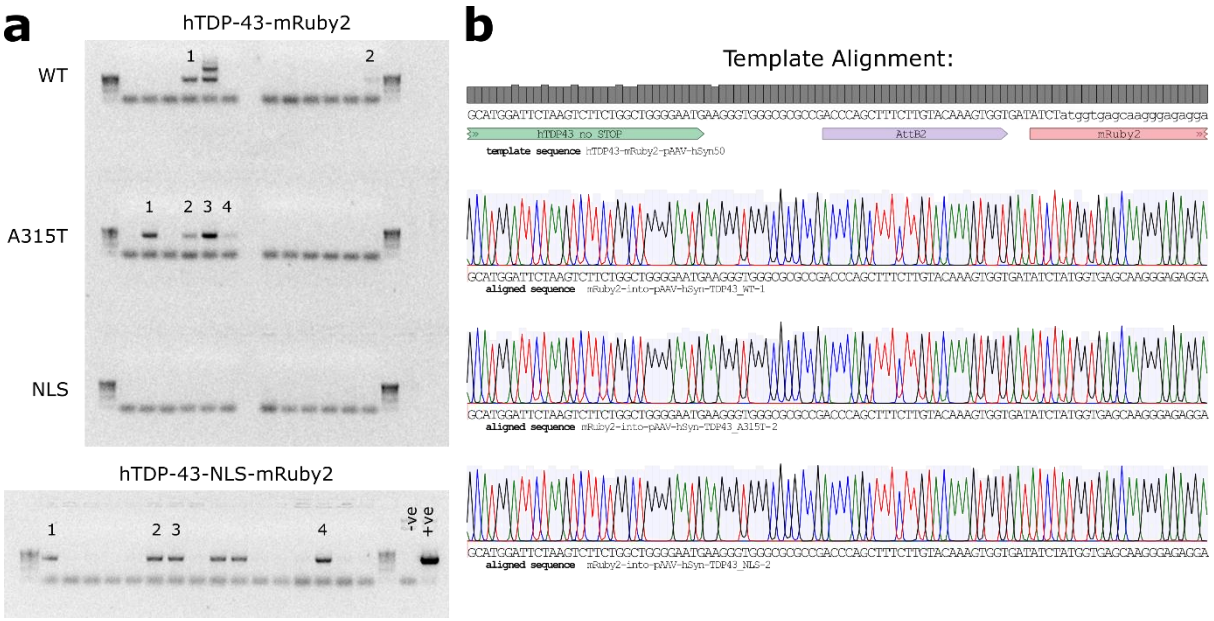

Supplementary 2: Results from cloning. **a.** Colonies containing pAAV-hSyn-hTDP43-mRuby2 were identified by colony PCR using mRuby2 primers; marked colonies were sent for Sanger sequencing. **c.** Sample of sequencing results, showing the linker window between hTDP-43 and mRuby2. From top to bottom hTDP43-WT-mRuby2 clone 1, hTDP43-A315T-mRuby2 clone 2, and hTDP43-ΔNLS-mRuby2 clone 2 were selected for AAV production

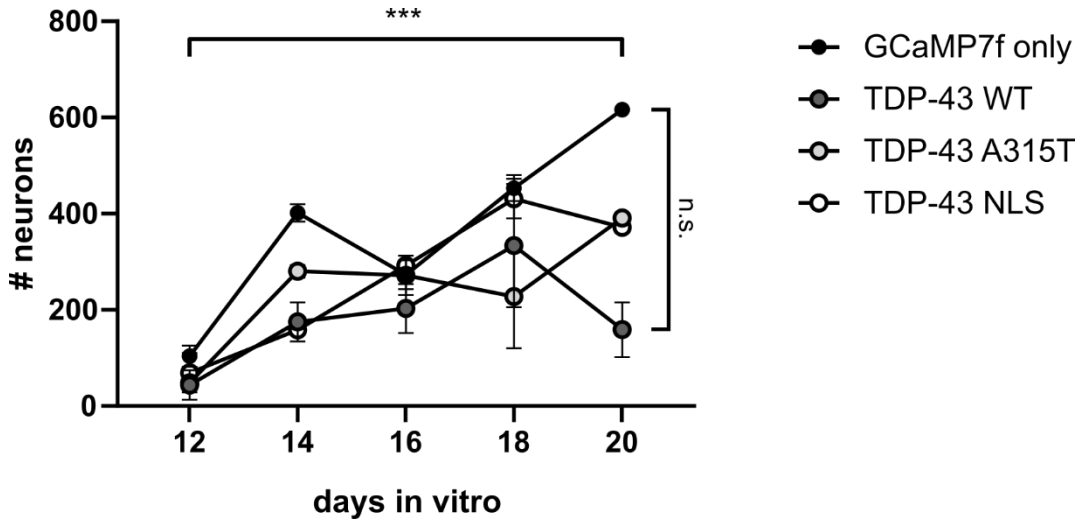

Supplementary 3: In cultures co-transduced with jGCaMP7f and TDP-43-myc variants or single transduced with jGCaMP7f, the number of neurons increased over time from 12 to 20 DIV. There was no significant difference in the number of neurons present between groups. (***, $p < 0.001$; n = 3 virally transduced wells in technical replicate).

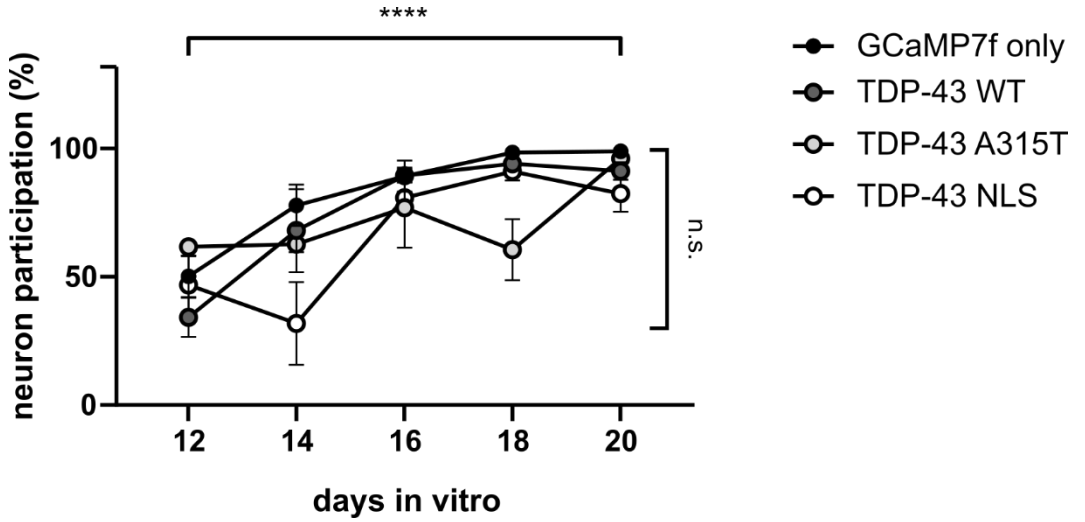

Supplementary 4: Cultures co-transduced with jGCaMP7f and TDP-43-myc variants or single transduced with jGCaMP7f were scored for neuronal participation in events. The percentage of total neurons participating in synchronised signalling events increased over time, with no significant difference between groups. (****, $p < 0.0001$; n = 3 virally transduced wells in technical replicate).

Supplementary 5: Sample pipeline for Miniscope data analysis.

In [1]:

```
import warnings
warnings.filterwarnings('ignore')
import numpy as np
from time import time
from matplotlib.pyplot import *

import matplotlib.animation as animation
import imageio
from IPython.display import HTML

import scipy
import glob
import yaml
import sys,os
import h5py as hd
from time import time
import av
#specific to miniscopy
from miniscopy.base.motion_correction import *
from miniscopy import setup_cluster, CNMFE,
      generate_data, get_default_parameters
```

In [2]:

```
folder_name= r"C:\Users\caiman_data\movies\miniscoPy"
files = glob.glob(folder_name+'/*.avi')
print (files)
```

```
['C:\\Users\\caiman_data\\movies\\miniscoPy\\msCam1.avi',
'C:\\Users\\caiman_data\\movies\\miniscoPy\\msCam2.avi']
```

loads parameters and starts the cluster

In [3]:

```
parameters = yaml.load(open('example_movies/parameters.yaml', 'r'))
c, procs, n_processes = setup_cluster(backend='local', n_processes=8,
single_thread=False)
```

MOTION CORRECTION

This function implements Normcorre (see...). All the outputs and associated information are stored in one HDF5 per session that will eventually be used for detection of calcium transients.

In [4]:

```
data, video_info = normcorre(files, procs, parameters['motion_correction'])
```

```
100%|██████████| 2/2 [00:08<00:00, 4.16s/it]
100%|██████████| 11/11 [04:01<00:00, 19.52s/it]
100%|██████████| 11/11 [04:03<00:00, 19.70s/it]
```

RUNNING CNMF-E

In [11]:

```
parameters['cnmfe']['init_params']['thresh_init'] =
1.0 parameters['cnmfe']['init_params']['min_corr'] =
0.2 parameters['cnmfe']['init_params']['min_pnr'] =
1.5

cnm = CNMFE(data, parameters['cnmfe'])
cnm.fit(procs)
```

```
100%|██████████| 20/20 [00:00<00:00, 313.33it/s]
100%|██████████| 20/20 [16:40<00:00, 46.39s/it]
100%|██████████| 20/20 [00:00<00:00, 161.96it/s]
100%|██████████| 9/9 [00:02<00:00, 3.72it/s]
100%|██████████| 20/20 [00:03<00:00, 6.03it/s]
100%|██████████| 10/10 [00:25<00:00, 2.58s/it]

No neurons merged!

Total time : 1158.8853    second
```

VISUALIZATION

In [12]:

```
procs.terminate()

cn, pnr = cnm.get_correlation_info()
```

```
100%|██████████| 126/126 [00:08<00:00, 7.20it/s]
100%|██████████| 480/480 [01:50<00:00, 4.38it/s]
100%|██████████| 125/125 [01:48<00:00, 1.17it/s]
```

Here all the spatial footprints (the A matrix) are normalized between 0 and 1 and the sum of all responses is then displayed.

In [13]:

```
dims = cnm.dims
C = cnm.C.value.copy()
A = cnm.A.value.copy()

# A is normalized to 1 for display
A -= np.vstack(A.min(1))
A /= np.vstack(A.max(1))
Atotal = A.sum(0).reshape(dims)

from matplotlib.pyplot import *
import matplotlib.gridspec as gridspec

tmp = Atotal.copy()
tmp[tmp == 0] = np.nan
figure(figsize = (20,10))
gs = gridspec.GridSpec(3,3)
subplot(gs[0:2,0])
imshow(Atotal, aspect = 'auto')
title("A (spatial footprints)")
subplot(gs[0:2,1])
imshow(cn, aspect = 'auto')
contour(np.flip(tmp, 0), origin = 'upper', cmap = 'gist_gray')
title("Local correlation")
subplot(gs[0:2,2])
imshow(cn, aspect = 'auto')
contour(np.flip(tmp, 0), origin = 'upper', cmap = 'gist_gray')
title("Peak to noise ratio")
subplot(gs[-1,:])
plot(C)

title("C")
show()
```

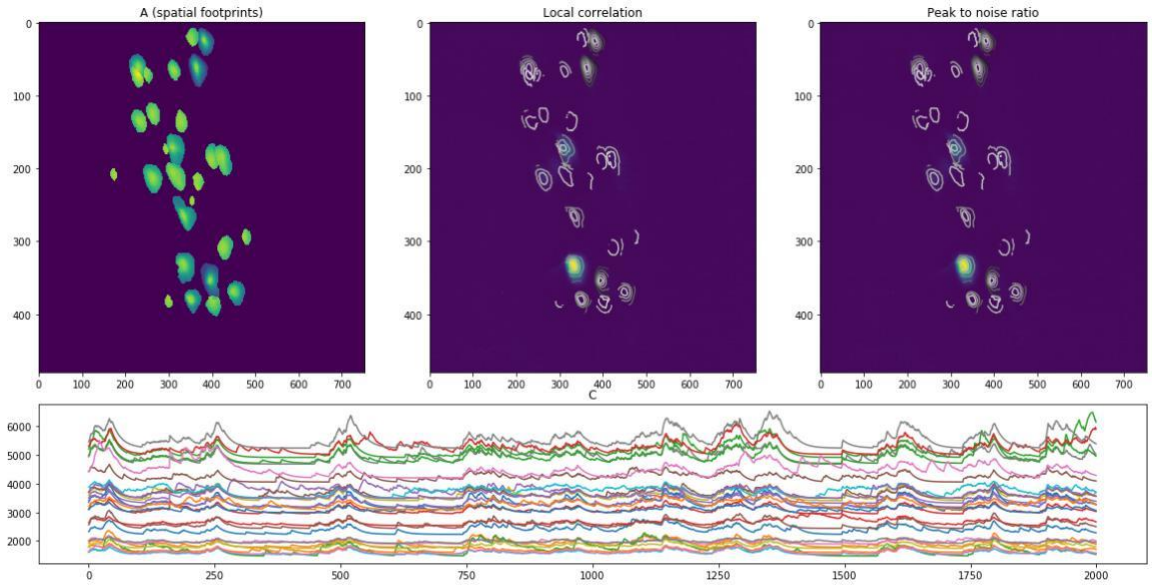

Selecting representative traces

The above code snippet maps out all identified traces onto the one plot, which quickly turns into a mess. In the block below, we iterate through removing excess traces, and select for eight representative traces

In [27]:

```
Cdel = C

for x in range (20):
    Cdel = np.delete(Cdel, 1, 1)
print (Cdel[[1]])
```

```
[[2339.2397 3223.0938 5247.3975 5335.1245 3745.5981 4440.41 4445.832
5513.8423]]
```

In [30]:

```
plot(Cdel)
# savefig('ctr-traces-3-rep.png', dpi = 300)
np.savetxt('ctr-out-3-rep.csv', Cdel, delimiter=',', fmt='%d')

show
```

Out[30]:

```
<function matplotlib.pyplot.show(*args, **kw)>
```

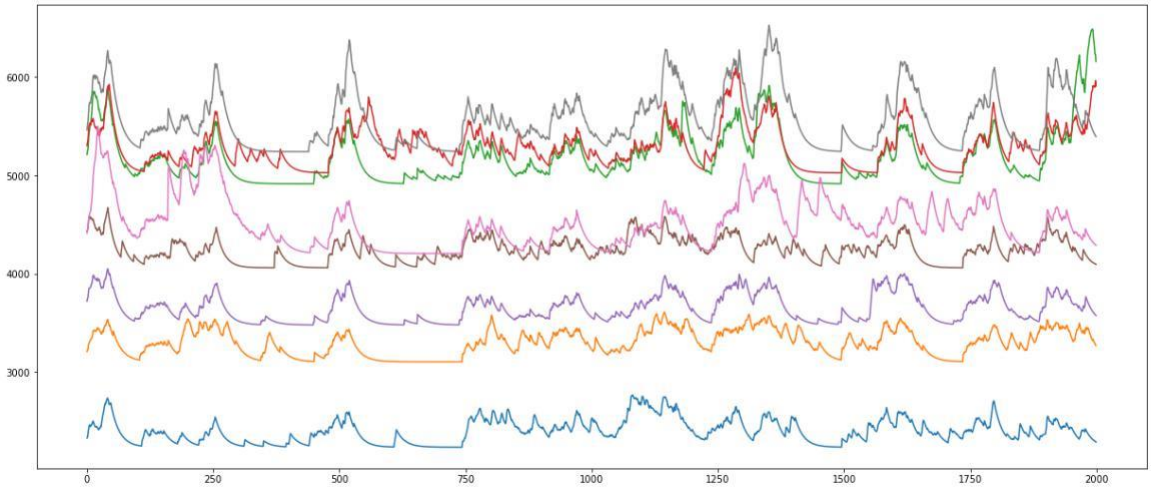

Supplementary 6: Overview of surgical sites tested, with rationale for choices made, and results obtained. Initially one animal was tested with each set of coordinates (Round 1-2). Numbers were increased when it became apparent that results were highly variable, even when using the same coordinates (3-5).

Round	Injection site 1[b, c]	Injection site 2[b, c]	Lens implant [b]	Mice	Rationale	Conclusions
1	-2.1, 2.1, 0.78	-	-2.1, 2.1, 0.7	1	Targeting the cortex at varying depths, as iTDP-43 mice show specific vulnerability of cortical regions (van Hummel et al,. 2018).	It is easy to damage the superficial layer of cortex. Cortical cells are not active under anaesthetic, which is useful to facilitate baseplate surgery. The Miniscope team recommends first targeting the hippocampus (Cai et al., 2016).
	-2.1, 2.1, 0.78	-	-2.1, 2.1, 0.5	1		
	-2.1, 2.1, 0.78	-	-2.1, 2.1, 0.3	1		
2	-3.6, 2.8, -3.2	-	-3.6, 2.8, -2.9	1	Target the ventral dentate gyrus, reports of anxiety effects (Anacker et al. 2018).	Targeting ventral hippocampus is too deep for the current GRIN lens. More GRIN lenses were purchased (6.1mm long, 0.5mm dia). Meanwhile, surgeries continued with Miniscope team coordinates; testing with both the original and adjusted coordinates.
	-3.16, 3.25, -3.85	-3.16, 3.25, -3.25	-3.16, 3.25, -3.25	1	Target ventral CA1, reports of anxiety effects (Jimenez et al., 2018).	
	-2.1, 2.1, 2.0	-2.1, 2.1, 1.7	-2.1, 2.1, -1.7	1	Miniscope team CA1 coordinates. To avoid aspiration, lens was implanted 0.4mm inferior.	
3[a]	**-2.1, 2.1, 2.0**	**-2.1, 2.1, 1.7**	**-2.1, 2.1, -1.7**	4	Adjusted Miniscope team CA1 coordinates.	Positive result from one control animal using the adjusted coordinated with no tissue aspiration. Surgeries continued with the adjusted coordinates
	-2.1, 2.1, 2.0	-2.1, 2.1, 1.7	-2.1, 2.1, -1.3 (with aspiration)	3	Original Miniscope team CA1 coordinates.	
4[a]	**-2.1, 2.1, 2.0**	**-2.1, 2.1, 1.7**	**-2.1, 2.1, -1.7**	8	Adjusted Miniscope team CA1 coordinates.	Positive result from one transgenic animal. Overall, coordinates showed a low success rate, with neurons just out of focus in two more mice.
5	-2.1, 1.7, -1.8	-2.1, 1.7, -1.6	-2.1, 2.1, -1.7	4	Viral injection sites moved superior, closer to lens implant.	No successful recordings were taken, although most animals showed high background fluorescence. Vibratome sections appear correct. Return to adjusted CA1 coordinates and repeat.
	-2.1, 1.7, -2 [d]	-2.1, 1.7, -1.4 [d]	-2.1, 2.1, -1.7	5	Continuous viral injection over a larger range.	
	-2.1, 1.7, -2 [d]	-2.1, 1.7, -1.4 [d]	-2.1, 2.1, -1.9	6	Continuous viral injection, with lowered lens implant position.	

[a] Coordinates which yielded a recording have been bolded.

[b] Injection and implantation site coordinates are of the form (AP, ML, DV).

[c] If one injection site is listed, 1µL was injected. If two injection sites are listed, 500nL was injected per site, unless marked.

[d] The syringe was gradually withdrawn from injection site 1 to site 2 over the 200 seconds of injection.